Implementation of UHPC Technology into the New England Construction Industry

(TIDC Project # 2.14)

Final Report
May 2025

Principal Investigator (PI): Kay Wille, Ph.D., Professor
Co-Principal Investigator (co-PI): Ramesh Malla, Ph.D., F. ASCE, F. EMI, Professor
Institution: University of Connecticut,
School of Civil & Environmental Engineering
Mailing Address: 261 Glenbrook Road, Unit 3037, Storrs, CT 06269-3037
Email: kay.wille@uconn.edu / ramesh.malla@uconn.edu
Phone: PI (860) 486-2074 / Co-PI (860) 486-3683
ORCID Number: PI 0000-0001-7398-3456 / Co-PI 0000-0002-8035-8402

Authors
Bijaya Rai, Ph.D. student
Mandip Dahal, Ph.D. student
Kay Wille, Ph.D., Professor
Ramesh B. Malla, Ph.D., Professor

Sponsored By
Transportation Infrastructure Durability Center
U.S. Department of Transportation, University Transportation Center Programs

TIDC
Transportation Infrastructure Durability Center
AT THE UNIVERSITY OF MAINE

THE UNIVERSITY OF MAINE | UMASS LOWELL | WESTERN NEW ENGLAND UNIVERSITY | WNE | UCONN UNIVERSITY OF CONNECTICUT | THE UNIVERSITY OF RHODE ISLAND | The UNIVERSITY of VERMONT

About the Transportation Infrastructure Durability Center

The Transportation Infrastructure Durability Center (TIDC) is the 2018 US DOT Region 1 (New England) University Transportation Center (UTC) located at the University of Maine Advanced Structures and Composites Center. TIDC's research focuses on efforts to improve durability and extend the life of transportation infrastructure in New England and beyond through an integrated collaboration of universities, state DOTs, and industry. The TIDC is comprised of six New England universities, the University of Maine (lead), the University of Connecticut, the University of Massachusetts Lowell, the University of Rhode Island, the University of Vermont, and Western New England University.

U.S. Department of Transportation (US DOT) Disclaimer

Acknowledgements

Funding for this research is provided by the Transportation Infrastructure Durability Center at the University of Maine under grant 69A3551847101 from the U.S. Department of Transportation's University Transportation Centers Program. The principal and co-principal investigator of the project would like to gratefully acknowledge and thank the following individuals and organizations whose support (financial, material, and/or in-kind) assisted in this research and significantly contributed to the success of the project:

Graduate and undergraduate assistants involved in this project:

Bijaya Rai, Ph.D. student
Mandip Dahal, Ph.D. student
Dominic Parciasepe, Undergraduate student
Cameron Larkin, Undergraduate student
Nathan Comment, Undergraduate student
Harley Jeanty, Undergraduate student

State Department of Transportation:

Connecticut Department of Transportation (CT DOT), Newington, CT, for their in-kind support.

Project Technical Champions:

We thank the technical champions for their insightful feedback throughout the project.

Messrs. Andrew Cardinali, P.E. and Bao Chuong, P.E. CT DOT, Newington, CT

Industry for supplying materials:

Bekaert fiber, HiPer fiber, Boral Flyash, Lafarge Holcim Cement, Steelike Concrete, Holcim Premix, Norchem, Tilcon and Chryso Inc.

Last, but not least, the University of Connecticut, its School of Civil and Environmental Engineering (SoCEE), the Advanced Cementitious Materials and Composites (ACMC) laboratory, and the Connecticut Transportation Institute (CTI) for cost share, in-kind support, laboratory facilities, and project administration help.

Technical Report Documentation Page

1. Report No.	2. Government Accession No.	3. Recipient Catalog No.
4. Title and Subtitle **Implementation of UHPC Technology into the New England Construction Industry (TIDC Project 2.14)**		5. Report Date 05/30/2025 6. Performing Organization Code
7. Author(s) Bijaya Rai, Mandip Dahal Kay Wille - https://orcid.org/0000-0001-2345-6789 Ramesh B. Malla - https://orcid.org/0000-0002-8035-8402		8. Performing Organization Report No.
9. Performing Organization Name and Address University of Connecticut 261 Glenbrook Rd Storrs, CT 06269-3037		10. Work Unit No. (TRAIS) 11. Contract or Grant No.
12. Sponsoring Agency Name and Address U.S. DOT Region 1 University Transportation Center (UTC) -Transportation Infrastructure Durability Center (TIDC), ASCC, University of Maine, 35 Flagstaff Rd., Orono, Maine, U.S.A.		13. Type of Report and Period Covered Final Report 10/01/2021-09/30/2024 14. Sponsoring Agency Code
15. Supplementary Notes		

16. Abstract

This research focuses on the long-term stability and durability of newly developed, resource-efficient non-proprietary ultra-high performance concrete (UHPC), advancing material design and development to support field implementation in structural transportation projects across New England. The study drives innovation in durability testing and results analysis, addressing critical gaps in performance assessment to facilitate the use of non-proprietary UHPC in bridge components and connections. This work builds upon the foundational efforts of previous US DOT UTC-TIDC Project 2.5: “Development and Testing of High/Ultra-High Early Strength Concrete for Durable Bridge Components and Connections."

17. Key Words	18. Distribution Statement		
Absorption, Drying Shrinkage, Durability, Electrical Surface Resistivity, Freeze-Thaw (F-T), Techno-Economic Analysis (TEA), Ultra-High-Performance Concrete (UHPC)	This document is available for public reference.		
19. Security Classification (of this report) Unclassified	**20. Security Classification (of this page)** Unclassified	**21. No. of pages** 43	**22. Price**

Form DOT F 1700.7 (8-72)

Table of Contents

List of Figures

List of Tables

List of Key Terms

Abbreviation	Definition
A&A	Andreasen and Andersen
AASHTO	American Association of State Highway and Transportation Officials
A/C	Aggregate to Cement Ratio
A/P	Aggregate to Paste Ratio
A/P_o	Aggregate to Powder Ratio
ACI	American Concrete Institute
ASCE	American Society of Civil Engineers
ASTM	American Society for Testing and Materials
B	Basalt
BS	British Standard

bwoc	by weight of cement
C_3S	Tricalcium Silicate
C_2S	Dicalcium Silicate
C_3A	Tricalcium Aluminate
CH	Calcium Hydroxide
C-S-H	Calcium-Silicate-Hydrate
CSA	Calcium Sulpho-Aluminate
CFP	Carbon Footprint
CTDOT	Connecticut Department of Transportation
DOT	Department of Transportation
FA	Fly Ash
FB	Fine Basalt
FHWA	Federal Highway Administration
F-T	Freeze-Thaw
GGBS	Ground Granulated Blast Furnace Slag
HRWR	High Range Water Reducer
LVDT	Linear Variable Differential Transformer
M	Reference UHPC Matrix
M-0.2SF	UHPC Matrix with 20% Silica Fume
M-RGP	UHPC Matrix with Recycled Glass Powder
M-0.3GGBS	UHPC Matrix with 30% of Cement Replaced by GGBS
MOE	Modulus of Elasticity
OPC	Ordinary Portland Cement
PC	Portland Cement
PSD	Particle Size Distribution
R	Resource Efficiency Factor
RCPT	Rapid Chloride Penetration Test
RDME	Relative Dynamic Modulus of Elasticity
RGP	Recycled Glass Powder
RPC	Reactive Powder Concrete
SF	Silica Fume
SCM	Supplementary Cementitious Materials
SPL	Superplasticizer
TIDC	Transportation Infrastructure Durability Center
UHPC	Ultra-High Performance Concrete
U.S.	United States
V_f	Fiber Volume Fraction
χ_f	Fiber factor
W/B	Water to Binder Ratio
W/C	Water to Cement Ratio
W/F	Water to Fines Ratio

Abstract

This research investigates the long-term durability and stability of newly developed, resource-efficient non-proprietary ultra-high performance concrete (UHPC) to facilitate its broader application in structural transportation projects across New England. Building on the foundational work of previous US DOT UTC TIDC Project 2.5 titled" Development and Testing of High/Ultra-High Early Strength Concrete for Durable Bridge Components and Connections," this current research project addresses critical barriers to widespread UHPC adoption, such as high material costs, limited flexibility in proprietary mixes, and the need for enhanced quality control. By developing cost-efficient, adaptable UHPC formulations, this research aims to bridge the gap between the laboratory advancements and the large-scale implementation, offering a sustainable solution for aging infrastructure.

Comprehensive durability testing of developed UHPC formulations was conducted in accordance with ASTM standards, focusing on chloride ion penetration (via electrical surface resistivity), drying shrinkage, freeze-thaw resistance, and absorption. These properties were monitored over the course of a year to capture both transient and steady-state performance. A durability assessment factor (κ) was introduced to evaluate and compare non-proprietary UHPC formulations. Results demonstrated exceptional performance of the developed UHPC formulations, with electrical resistivity exceeding the low chloride ion penetration threshold of 21 kΩ·cm within one week, no degradation after 600 freeze-thaw cycles, drying shrinkage below 0.1%, and absorption under 1.4%. Service life modeling projects a design life surpassing 350 years, aligning with or exceeding the performance of proprietary UHPC products.

In addition to laboratory evaluations, the study involved mixing UHPC in larger volumes to ensure the practical applicability of the developed UHPC mixes in preparation for field implementation. Information from this study about non-proprietary UHPC technology was disseminated through technical presentations at conferences and conventions, as well as through published conference articles and high-impact journal papers. Knowledge transfer was further supported through educational initiatives, including training for middle and high school students, teachers, and undergraduate students in UHPC mixing and testing processes.

This research not only advances the development and implementation of non-proprietary UHPC but also promotes long-lasting, cost-efficient solutions to extend the service life of bridge components and address the growing demands of aging infrastructure like reduced maintenance cost, reduced safety risk and resilient structures.

Chapter 1: Introduction and Background

1.1 Project Motivation

Concrete material has been used for building a wide range of infrastructure. Therefore, its durability is essential to ensure the longevity of infrastructure to withstand ever present environmental factors while maintaining its mechanical integrity. Key environmental factors (stressors) include freeze-thaw cycles, chemical attacks from sulfates and winter deicing salts, as well as physical wear and tear through abrasion. The durability of concrete directly correlates with the lifespan of structures, making the development of advanced, resilient materials a critical focus for the construction industry.

The aging and deteriorating infrastructure in the United States remains a pressing concern. The American Society of Civil Engineers (ASCE) assigned a C- rating to U.S. infrastructure in 2021, reflecting a modest improvement from the long-standing D+ rating [1]. Despite this progress, ASCE estimates that addressing infrastructure deficiencies will require $3.3 trillion, with a $1.4 trillion funding gap [2] . Without intervention, these deficiencies could lead to a projected $4 trillion loss in GDP by 2025 [2]. Among the primary factors contributing to the degradation of infrastructure are the corrosion of steel reinforcement and concrete deterioration caused by invasive ions.

Ultra-high performance concrete (UHPC) represents a transformative advancement in construction materials, offering unparalleled durability and mechanical strength. Characterized by a water-to-cementitious ratio below 0.2 and compressive strengths exceeding 150 MPa (22 ksi), UHPC exhibits exceptional resistance to chloride, sulfate, and chemical penetration [3]. The incorporation of discontinuous steel fibers further enhances ductility, mitigating crack propagation and extending the service life of structures [3]. This dense, low-permeability matrix ensures superior performance in aggressive environments, positioning UHPC as a leading solution for infrastructure challenges.

However, the widespread adoption of UHPC is hindered by high material costs and the proprietary nature of commercially available formulations. The previous research "Project 2.5: Development and Testing of High/Ultra-High Early Strength Concrete for Durable Bridge Components and Connections" completed under the US DOT UTC – TIDC program addressed these limitations by developing non-proprietary UHPC mixes using locally sourced materials [4]. These mixes have demonstrated excellent workability and compressive strengths, surpassing 150 MPa.

Building on the success of that research, this study focused on further optimizing UHPC formulations emphasizing durability testing, large-scale mixing, and knowledge transfer. By advancing the design and deployment of innovative concrete materials, this research aimed to significantly enhance the durability and extend the lifespan of transportation infrastructure, aligning with the objectives of Thrust Area 2 "New Materials for Longevity and Constructability" of the US DOT -TIDC program.

1.2 Research Goal and Objectives

The primary goal of this research was to develop and evaluate the long-term durability and stability of resource-efficient, non-proprietary ultra-high performance concrete (UHPC) to enable its broader application in transportation projects, thereby enhancing the longevity and resilience of aging infrastructure across the New England region.

In pursuit of this overall research goal, the following three objectives were defined:

1. Durability Testing and Performance Evaluation:
    - Conduct comprehensive durability assessments in accordance with ASTM standards, focusing on chloride ion penetration, drying shrinkage, freeze-thaw resistance, and absorption to evaluate long-term stability.
    - Introduce and apply a durability assessment factor (κ) to benchmark and compare the performance of non-proprietary UHPC with existing commercial alternatives.
2. Service Life Modeling and Large-Scale Testing:
    - Model the service life of the developed UHPC to estimate its performance, targeting a design life exceeding 350 years, and conduct large-scale mixing trials of 30 liters volume for potential field implementation.
3. Knowledge Transfer and Industry Outreach:
    - Facilitate educational initiatives by engaging middle and high school students, teachers, and undergraduate students in UHPC mixing and testing.
    - Disseminate research findings through technical presentations, high-impact journal publications, conference articles, and providing seminars to promote the adoption of non-proprietary UHPC in the construction industry.

By achieving these objectives, the research aimed to bridge the gap between laboratory advancements and large-scale infrastructure applications, contributing to more sustainable and durable transportation systems.

1.3 Report Overview

This report is organized into four chapters as follows:

- **Chapter 1** provides a general introduction, outlining the background, motivation, goal and objectives of the study.
- **Chapter 2** provides information about the materials used, experimental design and testing procedures.
- **Chapter 3** presents and analyzes the test results, with in-depth discussions interpreting the findings and their implications.
- **Chapter 4** provides the conclusions and a concise summary of the research outcomes.

Chapter 2: Methodology

2.1 Properties of Materials Constituents

Ordinary Portland cements type II/V (C II/V) was selected for its low C_3A content (4%) which was less than 8% as per recommendation from Sakai et al. 2008 [5], satisfying ASTM C150 [6], as well as its low Blaine value of 401 m^2/kg. Grey un-densified silica fume (SF) was selected based on median particle size (D_{50} = 0.5 µm) and low carbon content (0.3%). Fly ash class C (FA C), containing calcium oxide (CaO) greater than 18% as per ASTM C618 [7], was selected with median particle size (D_{50} = 11.3 µm). Recycled glass powder (RGP) of type GS was used based on its local availability and its favorable particle size (D_{50} = 9.4 µm) which fill the particle size gap between SF and cement. Similarly, based on activity test, grade 120 GGBS with median particle size (D_{50} = 11.6 µm) was used in this research. Only one type of local aggregate, basalt sand (B), with a maximum particle size of 1.18 mm was included here. It was sieved to follow the modified Andreasen & Andersen (A&A) curve with a q-value of 0.37 for optimum packing density [8]. Regarding fiber (F) reinforcement, striated, round steel fiber of 13 mm and 19 mm in length and 0.2 mm in diameter, were used. The tensile strength and modulus of elasticity of the steel fiber were taken to be 2850 MPa and 210 GPa, respectively. The summary of these UHPC constituents is presented in **Table 1**.

Table 1: Summary of UHPC constituents used in this research

Ingredients	IDs	Properties	Size
OPC type II/V	**CII/V**	Moderate fineness, low C_3A, high $C_3S + C_2S$	$D_{50} \approx 25$ µm
Silica fume	**SF**	Un densified grey SF with low carbon content	D_{50} = 0.5 µm
Recycled glass powder	**RGP**	Type GS, white color	D_{50} = 9.4 µm
Fly ash C	**FA C**	Type C	D_{50} = 11.3 µm
Granulated glass blast-furnace slag	**GGBS**	Grade 120	D_{50} = 11.6 µm
Basalt sand	**B**	High strength & high modulus of elasticity, low water absorption	Less than 1.18 mm (modified A&A, q = 0.37)
High range water reducer	**HRWR**	Solid content = 29%	
Fiber	**F**	Smooth & straight steel fiber	13 mm & 19 mm long/ 0.2 mm dia.

The chemical compositions of cementitious materials are presented in **Table 2**.

Table 2: Chemical compositions of cementitious materials*

Chemical Compositions	C	SF	RGP	FA C	GGBS
SiO_2 (%)	20.3	96.1	72.8	34.3	
Al_2O_3(%)	4.00	4.40	1.74	18.1	11.4
CaO (%)	63.1	0.16	14.0	27.3	
MgO (%)	2.70	0.20	0.67	5.88	
K_2O (%)		0.37		0.38	
Fe_2O_3 (%)	3.60	0.18		5.70	
Na_2O (%)		0.03	10.9	1.81	
SO_3 (%)	3.00	0.12		2.11	0.10
CO_2 (%)	1.60				
$CaCO_3$ (%)	86.0				
Cl (%)		0.03			0.01
S (%)				2.06	0.80
Equivalent Alkalis (%)		0.27			0.50
Specific gravity	3.15	2.22	2.46	2.76	2.95

* Based on data from suppliers: Lafarge Holcim Cement, Norchem, Pozzotive Glass powder and Boral Flyash

2.2 UHPC mix designs

This research continues the previous work on designing resource-efficient, non-proprietary UHPCs using local materials [9]. The most promising UHPC matrices from prior research, known for their high resource efficient factor (*R*), were selected for the durability investigation [1].

Table 3 summarizes the mix designs and properties of four UHPC matrices and two fiber-reinforced UHPC and provides an overview of the optimized UHPC matrices and fiber-reinforced UHPCs selected for durability investigation. The reference UHPC matrix (M) uses ordinary Portland cement type II/V (PC II/V), un-densified gray silica fume (SF), fly ash class C (FA C), basalt (B), and high range water reducer (HRWR). The weight proportions of ingredients (PC: SF: FA C) for the reference mix are kept as 1:0.25:0.25 with an aggregate to cement ratio by weight (A/C) of 0.8, an aggregate to powder ratio (A/P_o) of 0.53, and a solid content of HRWR to cement ratio of 0.011. Additionally, to the reference matrix (M), the following three matrices were also investigated:

a) M-0.2SF: Uses 20% of SF by weight of cement (bwoc) instead of 25%, optimizing compressive strength and workability [9]. The W/C was reduced from 0.24 to 0.23 to maintain comparable spread values.

b) M-RGP: FA C was replaced by RGP in M-0.2SF. The W/C increased from 0.23 to 0.25 due to RGP's higher water demand. It uses 20% SF bwoc to compare directly with M-0.2SF.

c) M-0.3GGBS: Replaces 30% of cement weight with GGBS in the mix M, maintaining other proportions for optimal performance [9].

Table 3: Overview of optimized UHPC matrices and fiber reinforced UHPC

	UHPC Matrices				Fiber Reinforced UHPC			
IDs	**M**	**M-0.2SF**	**M-RGP**	**M-0.3GGBS**	**M-1.0%**	**M-1.5%**	**M-1.0%**	**M-1.5%**
C II/V (kg/m^3)	924	965	925	641	717	714	751	747
GGBS (kg/m^3)				275				
SF (kg/m^3)	231	193	193	229	179	179	188	187
[*]SCMs (FA C)	231	241	241 (RGP)	229	179	179	188	187
C: SF: SCM	1:0.25:0.25	1:0.20:0.25	1:0.20:0.25	(0.7+0.3[*]):0.25:0.25	1:0.25:0.25			
Total binder (kg/m^3)	1386	1399	1387	1375	1076	1071	1126	1120
Water (kg/m^3)	207	206	207	205	203	202	168	167
HRWR (kg/m^3)	34	36	34	34	27	27	28	28
B (kg/m^3)	747	747	747	747	1076	1070	1126	1120
F (kg/m^3)	-	-	-	-	79	118	79	118
W/C	0.24	0.23	0.25	0.24	0.29	0.29	0.24	0.24
A/C	0.81	0.77	0.81	0.81	1.5	1.5	1.5	1.5
Spread (mm)	282	305	268	301	278	265	253	245
***R*-factor**	1.36	1.44	1.26	1.41	1.32[+]	1.25[+]	1.67[+]	1.20[+]

[*]Supplementary cementitious material, [*] GGBS, [+]Based on cost boundary value: $cost_b$ = US$1000/m^3

Additionally, four fiber-reinforced UHPCs with striated fibers of 19 mm and 13 mm at fiber volume fractions (V_f) of 1% and 1.5%, respectively, were selected. The W/C ratios were 0.24 for two and 0.29 for other two fiber-reinforced UHPCs, achieving desired spread values of 280-340mm as recommended by Wille et al. [8], measured according to ASTM C 230/230M [10]. A resource efficiency factor (R) was calculated for each UHPC mixture based on their relative workability, compressive strength, cost, and carbon footprint (CFP) as per [9]. Furthermore, an additional mix was prepared for large scale mix of 30 liters which could mimic the field scale mix in laboratory setting. For this mix, a proportioning value of 1:1.2:0.2:0.25 for C: SF: FA C was used with w/c ratio of 0.26, and HRWR with solid weight ratio of 0.015 bwoc. The aggregates used for this mix had a maximum size of 2 mm. In addition, 2% striated fibers by volume having length of 13 mm were also used.

2.3 Testing Setups & Testing Procedures

2.3.1. UHPC mixing

A 20-quart capacity Hobart mixer was used to mix all UHPCs with its bi-rotary motion at three different speeds. The mixing procedure followed the UHPC mixing protocol [11]. First, SF and aggregates were mixed for five minutes at speed one (107 rpm) to break down potential aggregation. Next, PC and SCMs were added and mixed for another five minutes at speed one, without water. Water and one third of HRWR were added over one minute, followed by the remaining HRWR all at speed one. The mixer speed was then increased to speed two (198 rpm) until the mixture started to turn over, then returned to speed one for complete turnover at slower speed. Mixing continued for an additional five minutes at speed two. When fibers were added, the speed was reduced to one, and the mixer ran for two more minutes to ensure fibers dispersion.

For large scale mix, a planetary mixer was used using the same mixing steps, but at same uniform speed. In addition, to account for casting delay on site, two delay times were considered. For samples with delay, the freshly prepared mixture was kept idling for either one or two hours. Then, the UHPC was mixed for two minutes.

2.3.2. Sample preparation

For each mix, two large beams each of dimensions 76 mm×10 mm×406 mm, two small prisms of dimensions 25 mm×25 mm×305 mm), and two cylinders of size 76 mm diameter×152 mm length) were cast for F-T, shrinkage, and electrical surface resistivity testing, respectively. Samples were consolidated by vibrating for 2.5 minutes at a frequency of 3.5 Hz. About 30 minutes after casting, the molds were covered with plastic to avoid water evaporation. F-T beams and cylinders were cured in water at room temperature and RH greater than 95% while small prisms were air-dried at room temperature with RH below 50% after demolding. After 14 days of curing, F-T beams were transferred to the F-T chamber.

For large scale mix, first the workability of the UHPC was tested, 2-inch cubes and dog bones (see 2.3.5. Mechanical tests section below for figure) were cast for compressive and tensile strength tests. A flow chart describing the procedure of mixing and casting specimens for samples with different delay times is shown in **Figure 1**.

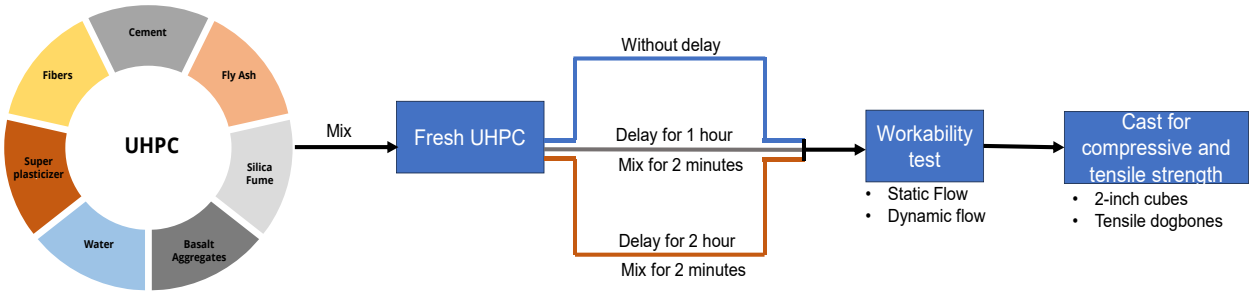

Figure 1: Overview of workflow for large scale mix.

2.3.3. Workability

For large scale mix, the workability of the UHPC was tested by its static and dynamic flow following ASTM C230/C230M [12]. The static flow was measured by lifting the cone vertically and allowing the mix to flow without any external mechanical disturbance to the fresh mix while the dynamic flow was measured on the flow table after lifting the cone vertically and dropping the table 25 times as per ASTM C1437 [13]. The flow measurement was taken in four directions, and the average value was reported.

2.3.5. Mechanical tests

For large scale mix, compressive strength at 7 days and 28 days were conducted following ASTM C109/C109M [14]. A loading rate of 30,000 lbs/min was used to fail the cubes within 4 minutes. In addition, dog bone-shaped specimens were cast to carry out direct tensile tests. The tensile strength was tested in displacement control at a loading rate of 0.6 mm/min [15]. Two LVDTs were attached on the sides to measure the displacements which were converted into strain by dividing the relative displacement by gauge length (80 mm). Figure 1 shows the setup for the direct tensile test and geometry of the tensile dog bone specimen. At least 3 samples were tested for both compressive and tensile strength and each of their average values was reported. **Figure 2** shows the setup for the direct tensile test and geometry of the tensile dog bone specimen.

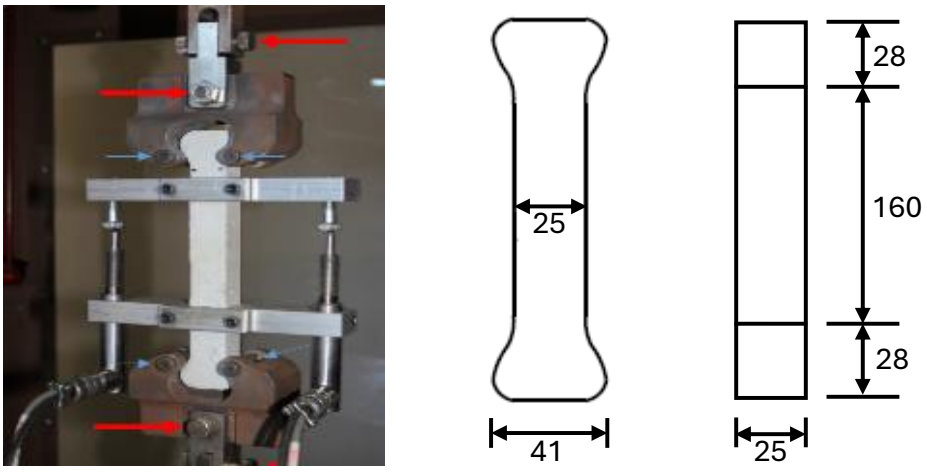

(a) (b)

Figure 2: Direct tensile test (a) Direct tensile test setup and (b) Geometry of tensile dog bone specimen (all dimensions in mm)

2.3.4. Absorption

The water absorption test was based on ASTM C642 [16]. The samples were cut into 2-inch slices and submerged in water for 48 hours. They were then prepared to achieve a saturated surface-dry (SSD) condition, weighed, and oven-dried at 100°C for 48 hours. After cooling for one hour, the samples were reweighed and oven-dried for an additional day. The following day, the samples were weighed again. If the weight change was less than 10% compared to the previous day, the drying process was concluded.

2.3.5. Electrical surface resistivity

Concrete surface resistivity tests were conducted to determine concrete permeability according to AASHTO TP95 [17]. The conceptual drawing and the test setup are shown in **Figure 3**. This non-destructive method monitors changes in resistivity over time, indicating the development of the concrete pore-structure [18]. The cylinders were demolded one day after casting and cured at room temperature and over 95% of RH. The test setup was modified to adjust 3 in×6 in (76 mm × 152 mm) cylinders which was originally designed for 4 in ×8 in (102 mm × 203 mm) cylinders. Two cylinders from each UHPC series were used to measure electrical surface resistivity. Measurements were taken at 0˚, 90˚, 180˚, and 270˚ on each cylinder as seen in **Figure 3(a)**. The average of these four measurements per cylinder was calculated to get representative value for each UHPC series. Resistivity was measured daily for the first months, every other day thereafter, and then weekly until the equipment's detection limit was reached.

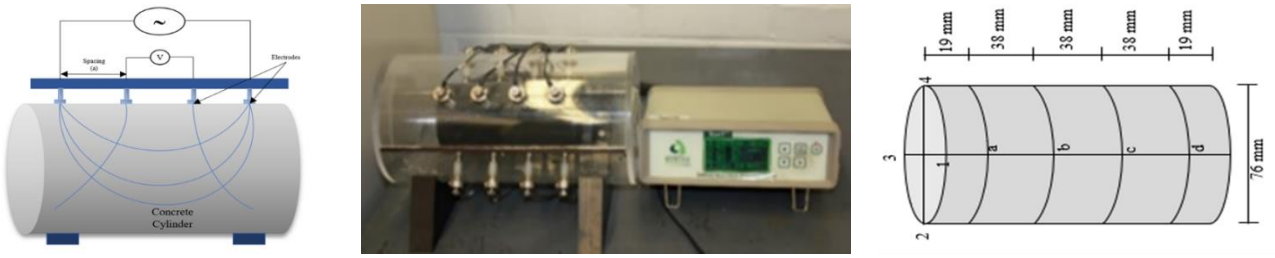

(a) Conceptual drawing of electrical surface resistivity [19] (b) Lab test set up (c) Specimen with test markings

Figure 3: Electrical surface resistivity

2.3.6. Shrinkage

Shrinkage is one of the major causes of cracking in hot and humid weather. Thus, it was measured by taking two small prisms (25 mm×25 mm×305 mm). These prisms are shown in **Figure 4**. A length comparator was used to measure long-term shrinkage as per ASTM C157/C157M-17 [20]. Each beam had shrinkage studs on both sides. These beams were demolded after one day and kept at room temperature with RH below 50%. Shrinkage measurements were taken daily for the first month, every other day subsequently, and then weekly to observe both transient and steady state behavior over the years. After one year, the samples were cured normally to observe any changes in length.

(a) Drying method (b) Shrinkage measurement

Figure 4: Drying shrinkage measurement (a) Drying method (b) Measurement method.

2.3.7. Freeze thaw durability

Freeze–thaw (F-T) testing is widely popular and mandated practice in the construction industry to evaluate concrete's resistance to F-T degradation, serving as an indirect assessment of material durability.

Two beams from each mix series were used for F-T testing as per ASTM C666 [21]. These beams were cured normally for 14 days and subjected to 600 F-T cycles, exceeding the ASTM requirement of 300 cycles. The samples were fully submerged in water-filled containers slightly larger than the sample size to reduce water volume as less water requires less time and energy to complete a cycle. The F-T chamber (**Figure 5)** facilitated thermal expansion and contraction during the cycles. The chamber was programmed to execute freezing and thawing cycles every 3 hours, with temperature limits of -23°C and 2°C (-9 ºF and 36 ºF), respectively. Resonance frequency and weight of beams were measured after every 30 cycles up to 600 F-T cycles.

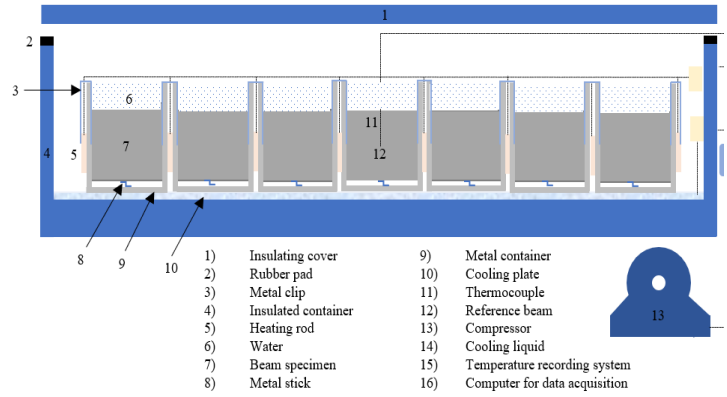

(a) Detailed drawing of F-T chamber

(b) F-T chamber

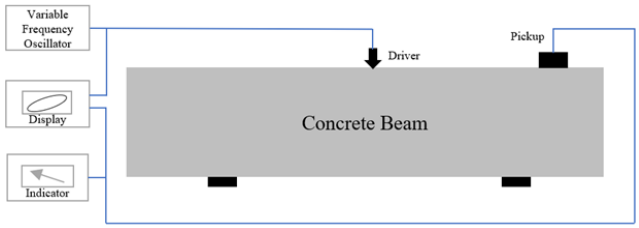

(c) Forced resonance measurement setup

(d) Resonace frequency testing

Figure 5: Freeze thaw chamber and resonance frequency measurement setup

The forced resonance frequency method was used to measure the resonance frequency of UHPC beams as per ASTM C215 [22]. An electro-mechanical driving unit forced the beam to vibrate, and a lightweight pickup unit monitored the response. The driving unit, activated by a variable frequency oscillator, generated vibrations that varied in resonance depending on the concrete quality. The driving frequency was adjusted until the measured response reached maximum amplitude. The frequency at which the maximum response occurred was recorded as the resonant frequency of the specimen. The following equations were used [22]:

Dynamic modulus of elasticity $E_{dyn} = CMn^2$ (1)

, where M = mass of specimen (kg), n= fundamental transverse frequency (Hz) and

$$C = 0.9464 \times \frac{L^3 T}{bt^3} \quad \text{m}^{-1} \text{ for a prism} \tag{2}$$

, where L, t and b are length, width, height of prism in meter, respectively.

The relative dynamic modulus of elasticity (RDME) was calculated as the ratio of the dynamic modulus at the nth F-T cycle to its initial value at zero F-T cycles:

$$RDME = \frac{n_1^2}{n^2} \times 100\% \tag{3}$$

, where n and n_1 are the fundamental transverse frequency at zero and nth F-T cycles.

The summary of the test details is presented in **Table 4** below.

Table 4: Summary of tests and their respective standards

Tests	Specimen Dimension	Standards
Workability	Fresh paste	ASTM C230/230M [10] and ASTM C1437 [13]
Compressive strength test	2-inch cubes	ASTM C109/109M [14]
Water absorption test	50 mm thick disk of 76 mm diameter	ASTM C642 [16]
Electrical surface resistivity	Cylinder of 76 mm diameter and 152 mm height	AASHTO TP95 [17]
Total shrinkage	Beam of 25 mm×25 mm×30 5mm	ASTM C157 [20]
Freezing & thawing durability	Beam of 76 mm×102 mm×406 mm	ASTM C666 [21]

Chapter 3: Results and Discussion

3.1 Workability

Flowability results of the UHPC mix at different times are shown in **Figure 6**. For the mixture without delay, the dynamic flow could not be measured because the flow exceeded 250 mm, the diameter of the table. After 1 and 2 hours of delay, the dynamic flow reduced to 215 mm and 185 mm, respectively. In the case of static flow, the flowability of the mix without delay was 276 mm which dropped by nearly 37% after 1 hour of delay to 175 mm and by almost 47% after 2 hours of delay to 148 mm. The drop in flowability is attributed to the initiation of setting and evaporation of water that occurred during the delay time.

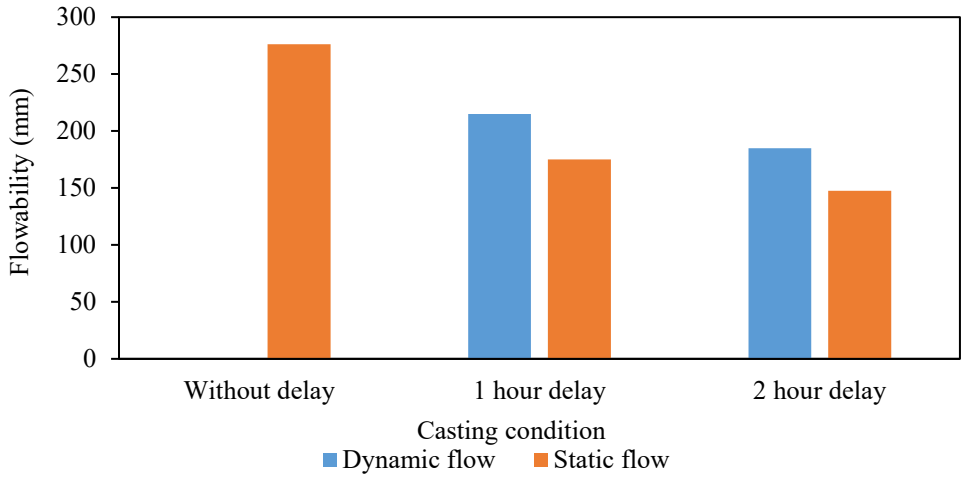

Figure 6: Flowability of the large-scale mix after different delay times

3.2 Mechanical tests

Compressive strength of the mix at different delay times is shown in **Figure 7**. The 7-day compressive strength for all samples exceeds 110 MPa. The average compressive strength of the mix without any delay was 115 MPa, while the samples after delay had an average compressive strength of 127 MPa. The 28-day strength of all samples exceeded 150 MPa. Samples without delay and 2 hours of delay had an average compressive strength of 155 MPa and 156 MPa while the sample with 1 hour of delay had an average compressive strength of 166 MPa. Interestingly, even after delay the compressive strength of samples did not decrease but rather increased for samples with 1 hour of delay.

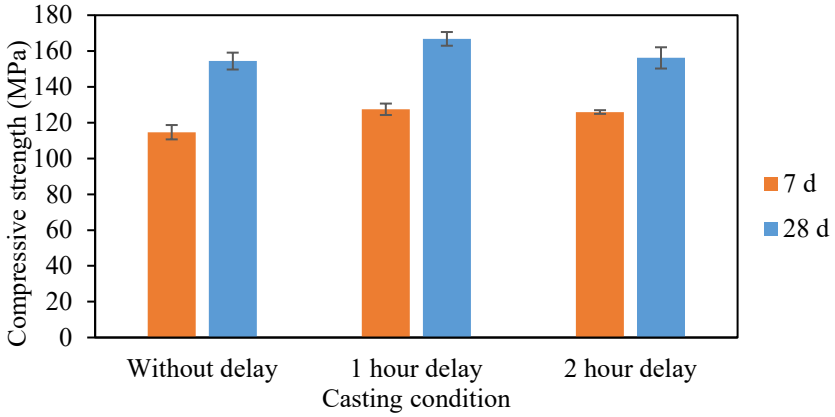

Figure 7: Compressive strength of large-scale mix after different delay times

The individual tensile stress-strain curves of samples and the average ultimate tensile strength are presented in **Figure 8**. All samples show ultimate tensile strength exceeding 11 MPa and exhibit strain-hardening behavior. The sample without delay has an average tensile strength of 14 MPa while the samples with one and two hours of delay have an average tensile strength of 14.5 and 11.6 MPa. The samples had an average hardening strain of 0.28%, 0.21%, and 0.23% for samples without delay, 1-hour delay, and 2 hours of delay, respectively.

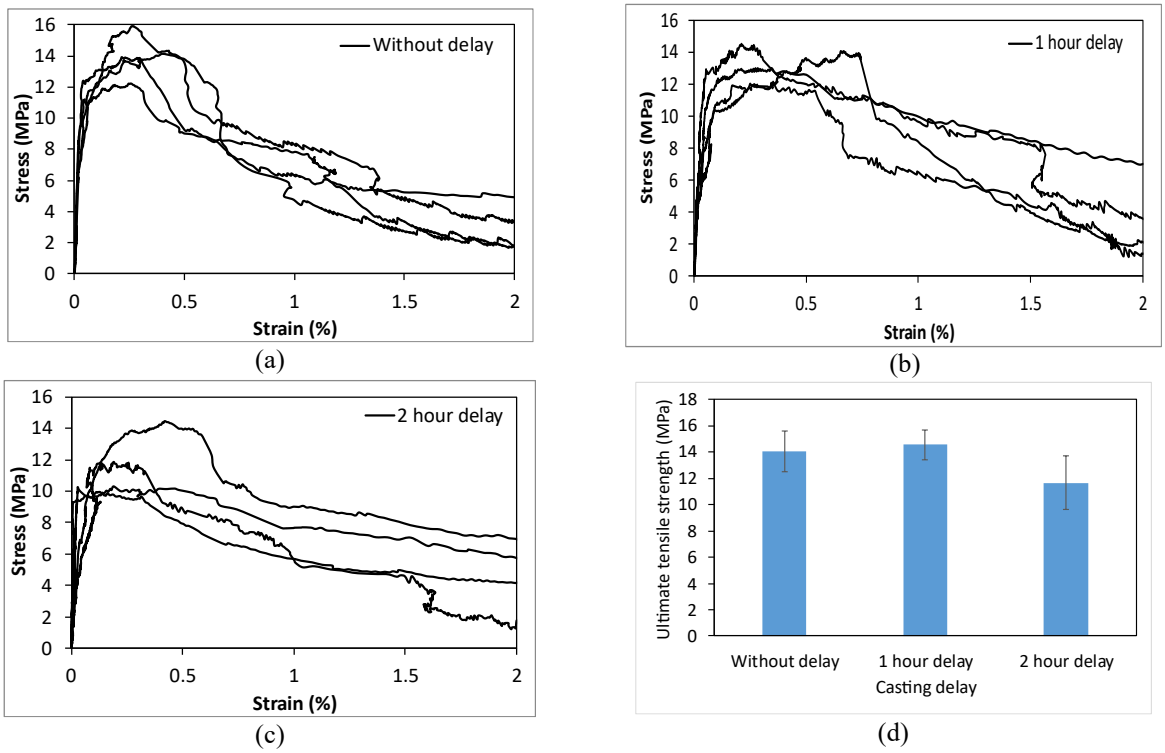

Figure 8: Individual tensile stress strain curves for samples (a) without delay, (b) 1-hour delay, and (c) 2-hour delay respectively, (d) ultimate tensile strength of samples

3.3 Absorption

Water absorption of 28-day UHPCs is presented in **Figure 9**. All four UHPCs exhibited less than 1.4% absorption, which is very low. Two commercial UHPC (represented as Comm. 1 and Comm. 2 in **Figure 9**) were tested for comparison. The results indicate that their absorptivity is comparable to the non-proprietary UHPCs. The very low water absorption is attributed to the dense microstructure and disconnected capillary pores [23–25].

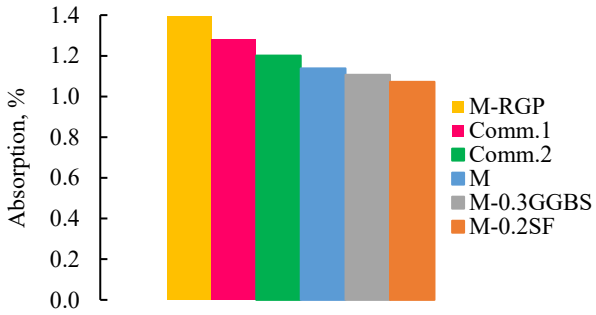

Figure 9: Absorption and its correlation with air content in UHPC

3.4. Electrical surface resistivity

The electrical surface resistivity test results of UHPCs are shown in **Figure 10** and **Figure 11**. The purple dashed lines in the figures represent the threshold for low ion penetration of 21 kΩ·cm and negligible ion penetration of 254 kΩ·cm [17], while the purple solid line indicates the instrument's detection limit. The experimental data suggests that a second-degree polynomial equation (given by Eq. 4 below) fits the resistivity data well:

$$\text{Electrical surface resistivity} \quad \rho = at^2 + bt + c \quad \text{in k}\Omega\cdot\text{cm} \tag{4}$$

, where t is time (days for normal curing or hours for steam curing) and a, b, c are fitting parameters (values provided in each graph). The fitted equations show a strong correlation between resistivity values and curing time, with R-squared values exceeding 0.98 for all graphs.

3.4.1. Resistivity of UHPC matrices without fibers

Figure 10 presents the electrical surface resistivity values of all four UHPC matrices without fibers, along with fitting parameters for **Equation 4**. M-RGP, M-0.2SF and M exceeded the low ion penetration threshold after 2 days and negligible ion penetration threshold in less than 10 days. In contrast, M-0.3GGBS required 4 days and 21 days, respectively, to reach these thresholds. All UHPC matrices displayed similar electrical surface resistivity to M-0.3GGBS, as GGBS takes time

to develop a denser microstructure. At any given time, M-0.3GGBS showed up to 75% of the electrical surface resistivity of reference mix M. GGBS delays hydration reaction in early age stages by reducing the maximum temperature rise, which suppresses the early formation of CSH, but increases its formation in the later stages [26,27]. The delay is due to the slow dilution of clinker content in the paste because of the limited pozzolanic activity of the metals [27]. Despite these differences, all UHPC matrices eventually reached the equipment's detection limit of 1000 kΩ·cm at their own time.

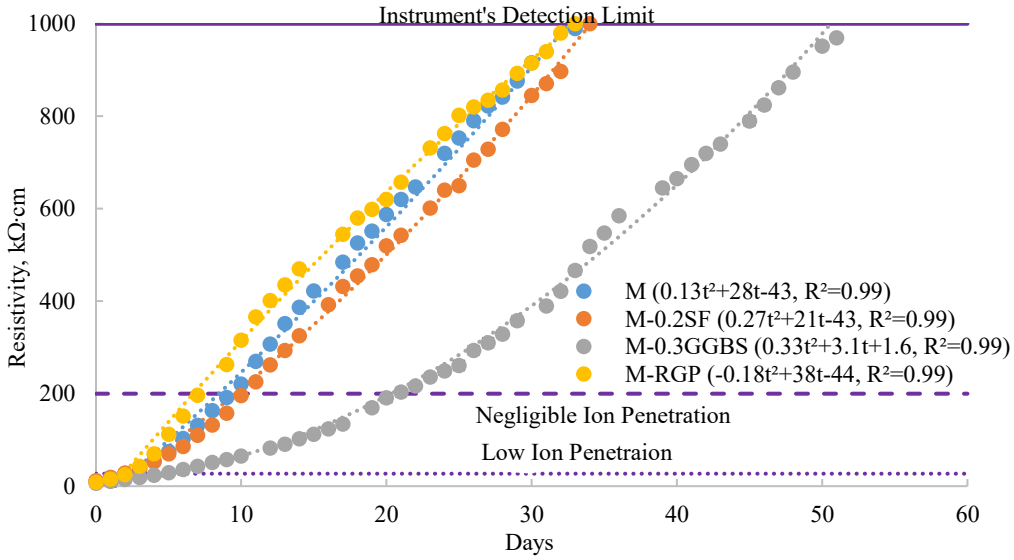

Figure 10: Electrical surface resistivity of newly developed non-proprietary UHPC matrices

Compared to M, M-0.2SF achieved electrical surface resistivity relatively slower, generally showing 14% less resistivity on any given measurement day.

Similarly, M-RGP exhibited a rapid increase in electrical surface resistivity compared to M and M-0.2SF, due to the presence of RGP instead of FA. This trend is consistent with steam curing as well [28]. Overall, M-RGP achieved up to 30% and 60% greater electrical resistivity compared to M and M-0.2SF, respectively, on any measurement day, although this increase slowed after a month.

3.4.2. Effect of fiber volume fraction in resistivity

Figure 11 presents the electrical surface resistivity of UHPCs with V_f of 1% and 1.5% at W/C of 0.24, the same as that of UHPC matrices without fibers. The UHPCs with fibers are denoted as M-1.0-0.24 and M-1.5-0.24 for V_f of 1% and 1.5%, respectively. The W/C and A/C ratios were kept constant to enable a direct comparison of UHPC with and without fibers, highlighting the effect of

steel fiber content on resistivity measurements. The measured resistivities of M-1.0-0.24 and M-1.5-0.24 are about 70-90% and 75-95% lower than those of M at comparable concrete ages. Previous research also found up to 70% reduction in electrical resistivity in fiber-reinforced conventional concrete compared to plain conventional concrete [29]. This significant reduction in resistivity, despite having the same matrix with the same W/C and A/C ratios, demonstrates the influence of steel fibers on resistivity measurements. Steel fibers being conductive, bridge the cementitious matrix and create pathways for electrical charges, resulting in an artificial decrease in electrical resistivity [30]. The increase in V_f indicates a higher number of steel fibers contributing to overall increased conductivity of the specimen, thereby decreasing the electrical surface resistivity [31].

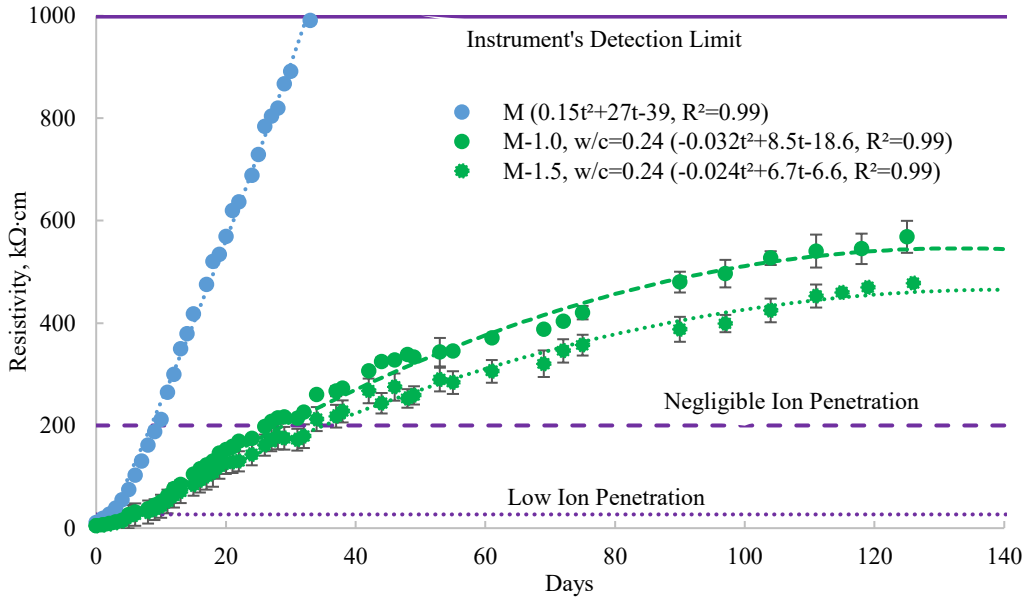

Figure 11: Electrical surface resistivity of newly developed non-proprietary UHPCs

3.4.3. Effect of W/C on resistivity

Figure 12 shows the electrical surface resistivity of UHPCs with W/C ratios of 0.24 and 0.29, represented by green and blue lines, respectively. Larger and smaller dashed lines denote UHPCs with V_f of 1.0% and 1.5%, respectively. An increase in W/C from 0.24 to 0.29 resulted in a decrease of 20%-65% for M-1.0 and 25%-80% for M-1.5. This indicates that a higher W/C ratio produces a more porous and permeable concrete matrix [32]. The increased porosity facilitates ion conduction within the concrete matrix, thereby increasing overall conductivity and reducing electrical resistivity.

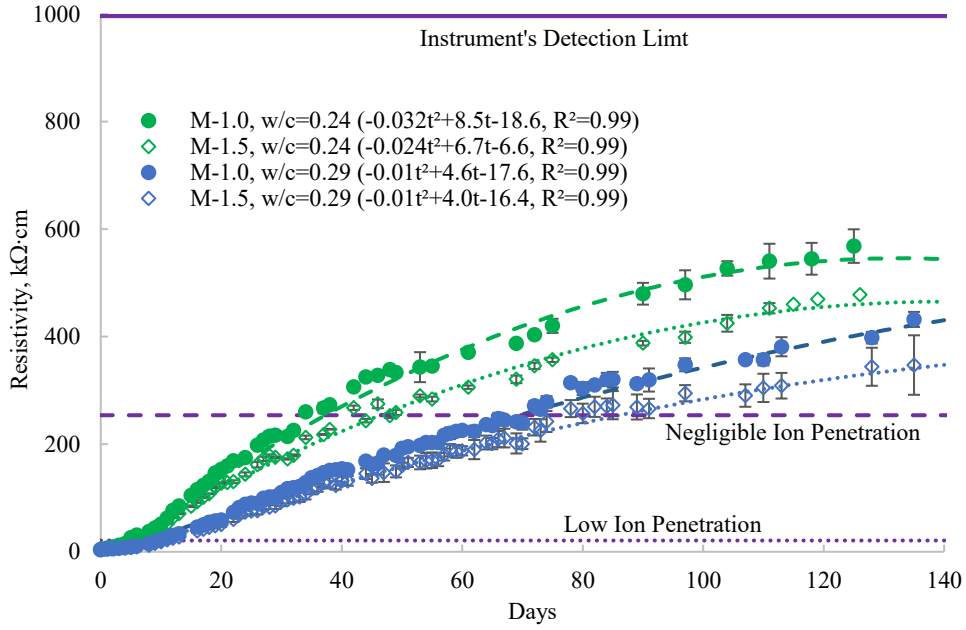

Figure 12: Electrical surface resistivity of newly developed non-proprietary UHPCs

3.4.4. Relationship between compressive strength and resistivity

Figure 13 shows the relationship between electrical surface resistivity and compressive strength. The parameters are empirically related by the formula from the curve fit:

$$\rho = 3.26 \times e^{0.03 \times f_c'} \quad (5)$$

, where ρ is the electrical surface resistivity in kΩ·cm and f_c' is the compressive strength in MPa. The strong correlation between these parameters is evidenced by an R-squared value of 0.88. Both electrical resistivity and compressive strength are linked to the density of the concrete matrix. This correlation suggests that improvements in matrix density positively influence both parameters.

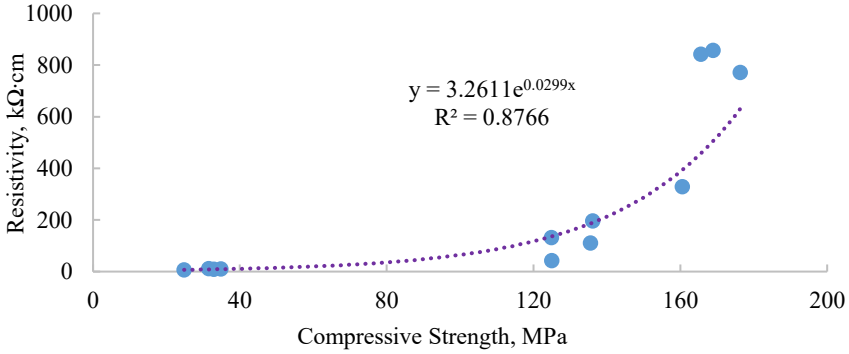

Figure 13: Relationship between electrical surface resistivity and compressive strength

3.4.5. Comparison of electrical surface resistivity results with other researchers

The highest 28-day electrical surface resistivity values from this research are compared to the highest values reported in previous studies, as discussed in the **Introduction**. **Figure 14** presents a summary of electrical surface resistivity results from previous studies [24,33–36]. Green dots represent the test results from non-proprietary UHPCs, while orange and yellow dots represent proprietary UHPCs. The figure clearly shows that almost all UHPCs achieved the low ion penetration threshold. However, only three studies, including the present one, achieved negligible ion penetration threshold within 28 days. Most previous studies did not measure electrical resistivity continuously, as done in this current research.

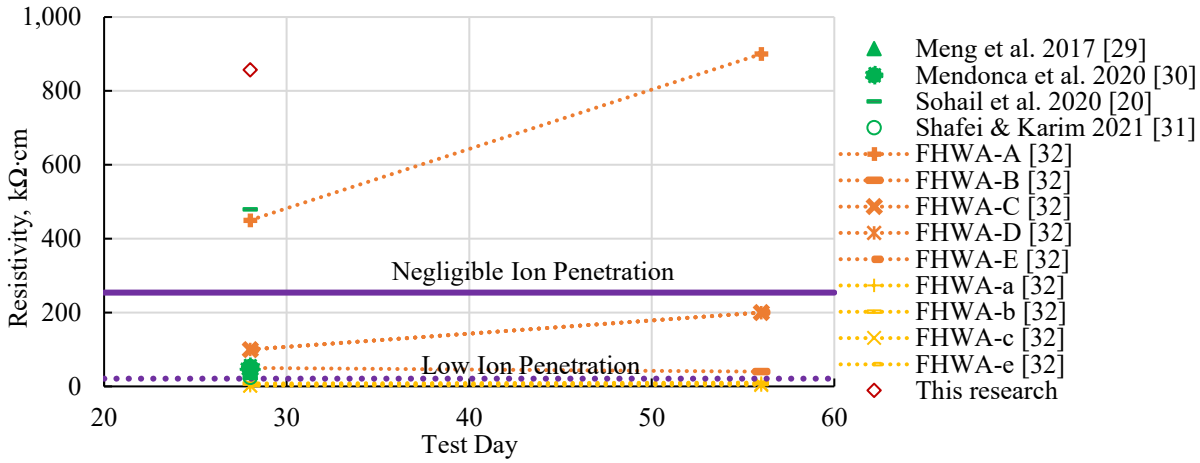

Figure 14: Summary of electrical resistivity results

3.5. Drying shrinkage

In this study, drying shrinkage is investigated in the UHPCs with and without fiber. Based on the experimental data, shrinkage can be predicted using **Equation 6**, which is best suited with the appropriate fitting parameters:

$$\text{Shrinkage, } \varepsilon(t)\% = \frac{t}{100\times(\alpha+\beta t)} \tag{6}$$

, where α, β are fitting parameters provided in the graphs, and t refers to the age of the concrete sample. The value of α determines the initial steepness of the shrinkage curve, while β determines the curvature in the subsequent stages.

3.5.1. Drying shrinkage in UHPC matrices

Figure 15 shows the drying shrinkage behavior and mass loss over time for all promising UHPCs dried at room temperature and below 50% RH. Shrinkage and mass change, both associated with moisture loss, are presented in **Figure 15(a)** and **Figure 15(b)**, highlighting their interrelation. These figures also show the prediction model with suitable fitting parameters alongside the experimental data. **Figure 15(a)** shows a steep drying shrinkage curve for up to one and half months, transitioning to an almost horizontal curve after reaching a steady state by two months. All UHPC matrices achieved drying shrinkage of less than 0.13% within two months, with no significant change observed even after a year.

Compared to the reference mix M, M-0.2SF exhibited up to 4% less strain, M-0.3GGBS up to 16% less strain, while M-RGP showed up to 30% more strain. Research suggests that increase GGBS replacement reduces both autogenous [37–39] and drying shrinkage slightly [37,40] as GGBS tends to maintain water content due to its hygroscopicity properties [40]. M-RGP showed relatively higher shrinkage compared to other UHPC matrices due to its higher W/C ratio (0.25 vs. 0.24). Drying shrinkage is sensitive to W/C ratio, with higher ratios resulting in greater shrinkage[25]. Both the commercial UHPCs showed less strain: Comm.1 exhibited up to 12% less strain and Comm.2 up to 23% less strain compared to M.

Unlike shrinkage, the mass loss graph remained steeper even after two months, becoming negligible after three months. This extended period to reach steady state is due to the ongoing hydration reaction utilizing available moisture and loss due to evaporation. Continuous hydration reduces pore size, increasing the surface tension among water molecules in finer voids, making moisture loss more difficult. Thus, the mass loss curve required more time to stabilize into a horizontal trajectory.

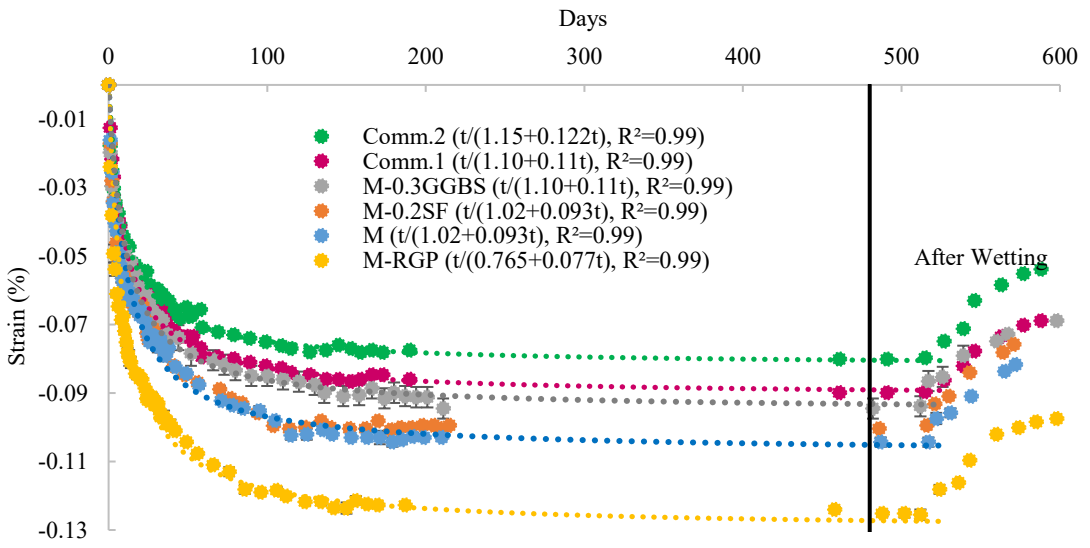

(a) Drying shrinkage

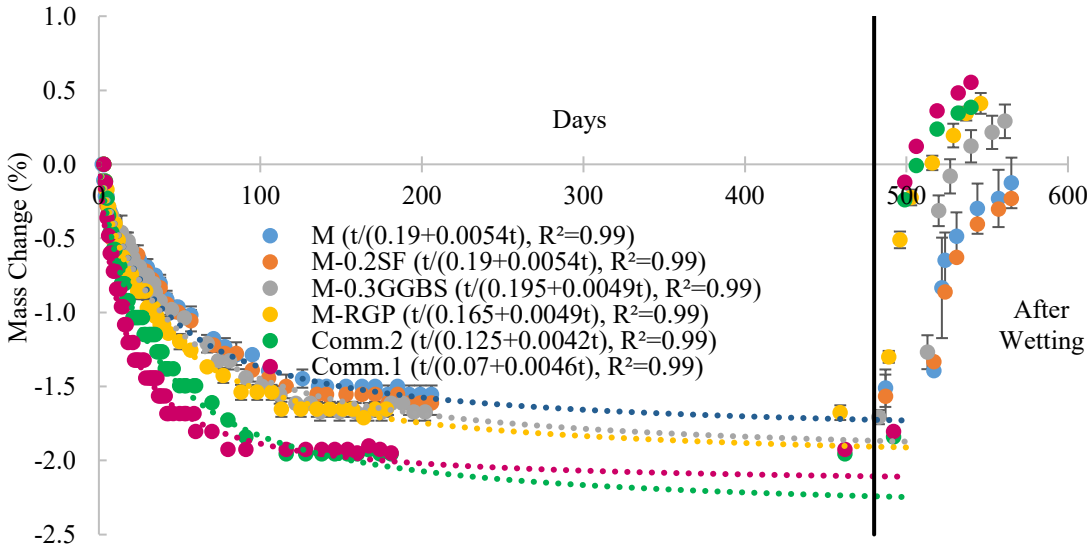

(b) Mass change

Figure 15: Drying shrinkage and mass change of UHPC matrices

3.5.2. Drying shrinkage in fiber reinforced UHPCs

Figure 16(a) compares the drying shrinkage of fiber-reinforced UHPCs at W/C ratios of 0.24 and 0.29 with the UHPC matrix (M) at W/C =0.24. There is a significant increase in shrinkage, up to 42%, when the W/C ratio increases from 0.24 to 0.29. A higher W/C ratio results in a less dense microstructure and increased water evaporation from the concrete, leading to greater shrinkage.

Figure 16(a) also shows that use of fibers in UHPC at the same W/C ratio can reduce shrinkage. Both fiber-reinforced UHPCs showed less drying shrinkage (ε = -0.0006 after 150 days) than compared to M (ε = -0.0009 after 150 days). The inclusion of fibers decreased shrinkage up to 45%. Increasing V_f from 1.0% to 1.5% further decreased the shrinkage by up to 7% for both the W/C ratios (0.24 and 0.29). Interestingly, the shrinkage of the reference matrix M is similar to that of fiber-reinforced UHPCs, even when W/C ratio changed from 0.24 (for M) and 0.29 (for M-1.0% and M-1.5%).

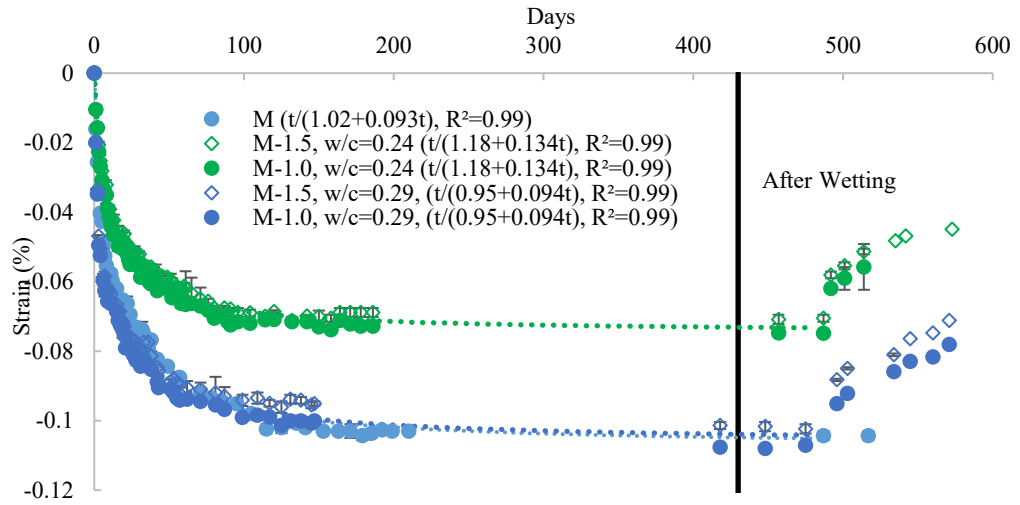

(a) Drying shrinkage

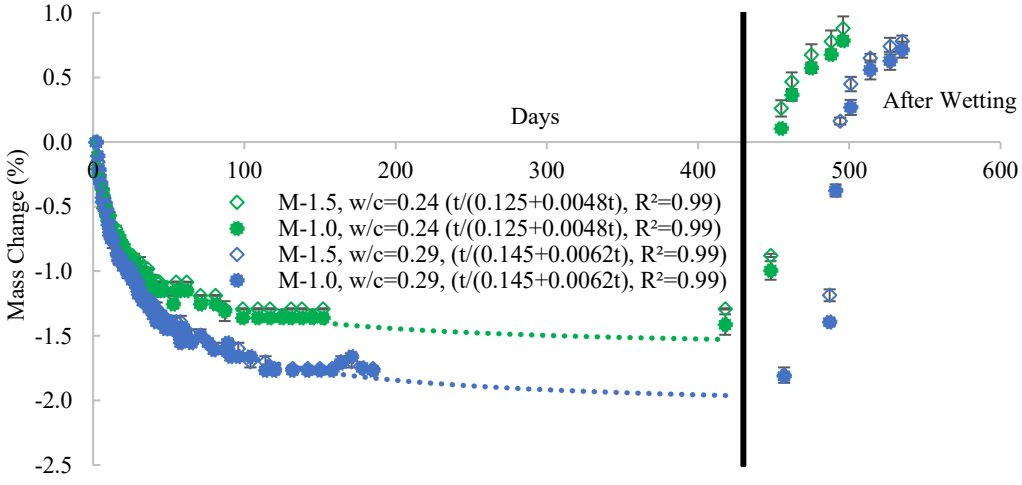

(b) Mass change

Figure 16: Drying shrinkage and mass change of fiber reinforced UHPCs

Figure 16(b) shows the mass change in fiber reinforced UHPC under drying shrinkage. It was observed that mass change is stable after 2.5 months of drying. The mass change in fiber reinforced UHPC with W/C of 0.29 is about 30% more mass loss than that with W/C of 0.24. It indicates that increase in W/C contributed to the mass loss in UHPC during drying shrinkage. It further correlates to the drying shrinkage as shown in **Figure 16(a)**.

3.3.3. Shrinkage behavior of steam cured UHPCs

Figure 17 shows the drying shrinkage behavior and mass loss of all steam cured UHPCs, which were dried after 24 hours of curing.

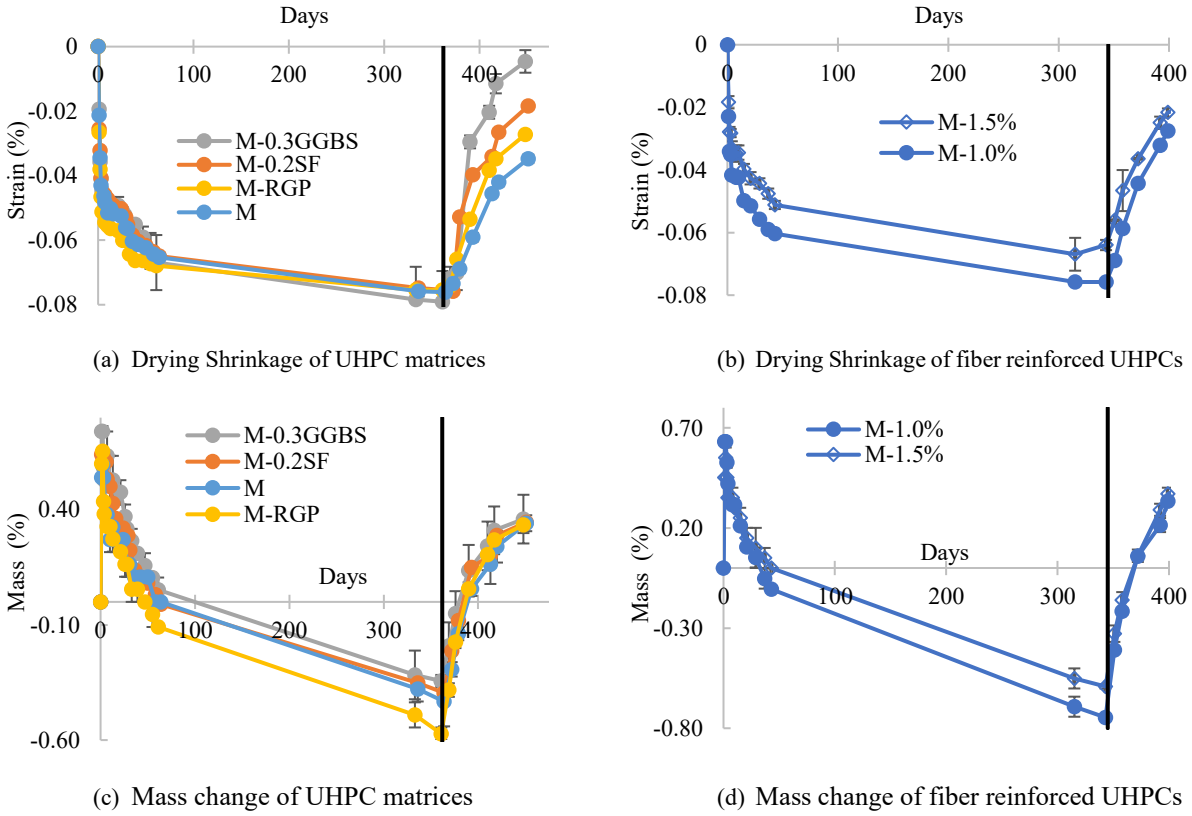

(a) Drying Shrinkage of UHPC matrices

(b) Drying Shrinkage of fiber reinforced UHPCs

(c) Mass change of UHPC matrices

(d) Mass change of fiber reinforced UHPCs

Figure 17: Drying shrinkage and mass change of steam cured UHPCs

Even during steam curing, all UHPC matrices exhibited shrinkage, as shown in **Figure 17(a)** and **Figure 17(b),** but gained mass due to extensive hydration by steam, as seen in **Figure 17(c) and Figure 17(d)**. Compared to **Figure 15** and **Figure 16,** steam curing reduced drying shrinkage: M showed up to 26% less, M-0.2SF up to 22% less, M-0.3GGBS up to 15% less, M-RGP up to 40% less, M-1.0% up to 20% less, and M-1.5% to 50% less strain values. This reduction is likely due to accelerated hydration reaction, which provides a very dense microstructure leading to mass gain. At

the same time, UHPC matrices achieved sufficient strength and stiffness, which restrained the shrinkage. The drying shrinkage caused by moisture loss was hindered due to finer capillary pores with higher surface tension among water molecules, preventing water evaporation from the pores. This is further supported by observations of water-cured UHPCs after a year of drying.

The authors have previously conducted similar studies, concluding that the inclusion of fibers significantly improves shrinkage resistance in steam-cured UHPCs [28].

3.5.4. Comparison of drying shrinkage results with other researchers

The lowest drying shrinkage values from this research are compared to those from previous studies, as discussed in the **Introduction** section. **Figure 18** presents a comparative summary of drying shrinkage results from previous studies [33–36,41–46], with green dots representing non-proprietary UHPCs and yellow dots representing proprietary UHPCs. The drying shrinkage values from this study are comparable to those in other studies. However, this is important to note that the shrinkage values in this study were measured after almost a year, whereas other studies measured them within a six-months period.

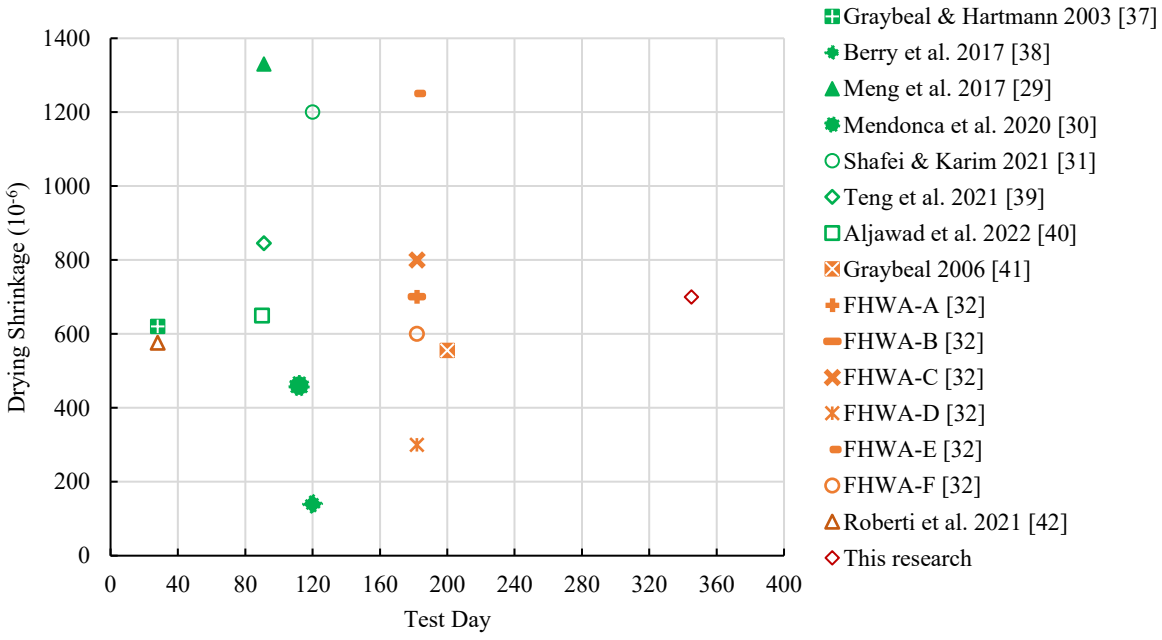

Figure 18: Comparative Summary of drying shrinkage of UHPCs

3.6. Freeze-thaw resistance

3.6.1. UHPC matrices

Figure 19 shows freeze-thaw (F-T) behavior of newly developed UHPC matrices. Interestingly, there is an increase in the dynamic modulus of elasticity (MOE) and mass, even under extreme F-T cycles. None of the UHPC matrices showed any signs of deterioration after 600 F-T cycles. This resistance to accelerated exposure is attributed to either a very dense microstructure or an efficient internal air void system. The relative dynamic modulus values are 102.3 for M-0.2SF, 103.2 for M-0.3GGBS, 105.1 for M, 103.5 for M-RGP after 600 F-T cycles. The dynamic MOE is highest for M-0.2SF, followed by M-0.3GGBS, M-RGP and M. M-0.2SF exceeded M by up to 5.9%, M-0.3GGBS by up to 3.3%, and M-RGP acted almost similar to M. Increase in dynamic MOE is supported by the mass gain which is about 0.1% after 600 F-T cycles.

These findings are corroborated by other studies [34]. The mass increase is due to the hydration of unreacted cementitious material during thawing cycles [47,48], where temperatures rise from 0 to 40°F [21]. Given the very low W/C ratio, not all cementitious material could hydrate during the initial 14-day curing period, continuing to hydrate during the thawing cycles. The formation of a denser microstructure through further hydration leads to an increase in the relative dynamic modulus over time. Such characteristics are typical of self-healing concrete, which can autonomously repair cracks and improve the overall resilience of structures.

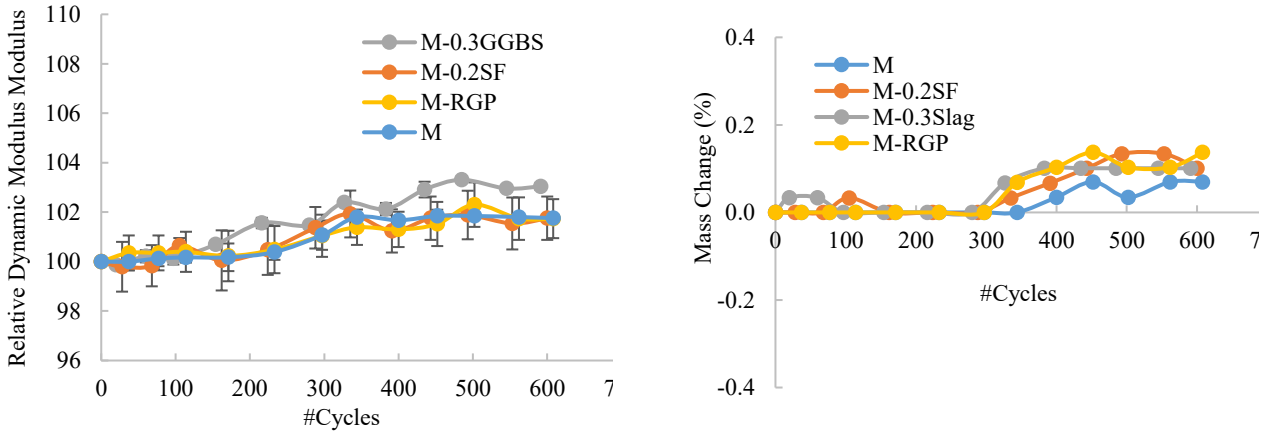

(a) Dynamic modulus of elasticity (b) Mass change (%)

Figure 19: Freeze-thaw resistance of UHPC matrices

3.6.2. Influence of W/C and fiber volume fraction

Figure 20 shows the F-T behavior of fiber-reinforced UHPCs with V_f= 1.0% and 1.5%, and W/C ratios of 0.24 and 0.29. Similar to UHPC matrices, there is no deterioration even after 600 F-T cycles. All fiber-reinforced UHPCs achieved a RDME greater than 100%: 101.8 for M-1.5-0.24, 102.2 for M-1.0-0.24, 101.4 for M-1.5-0.29, and 101.2 for M-1.0-0.29. The increase in dynamic MOE is supported by the corresponding increase in mass.

Although M, M-1.5-0.24 and M-1.0-0.24 have same W/C ratio of 0.24, M-1.5-0.24 and M-1.0-0.24 show higher dynamic MOE by up to 9.1% and 7.1%, respectively. This suggests that the addition of fibers might have increased the dynamic MOE. Previous research also demonstrated a 4.5% increase in dynamic MOE with the addition of fibers in UHPC [49].

Furthermore, M-1.0% and M-1.5% showed up to 2.3% and 3.1% increases in dynamic MOE at W/C = 0.24, compared to W/C = 0.29. This increase is attributed to a denser microstructure of the UHPC matrix influenced by the W/C ratio. However, there is no distinct difference in mass gain among these UHPCs.

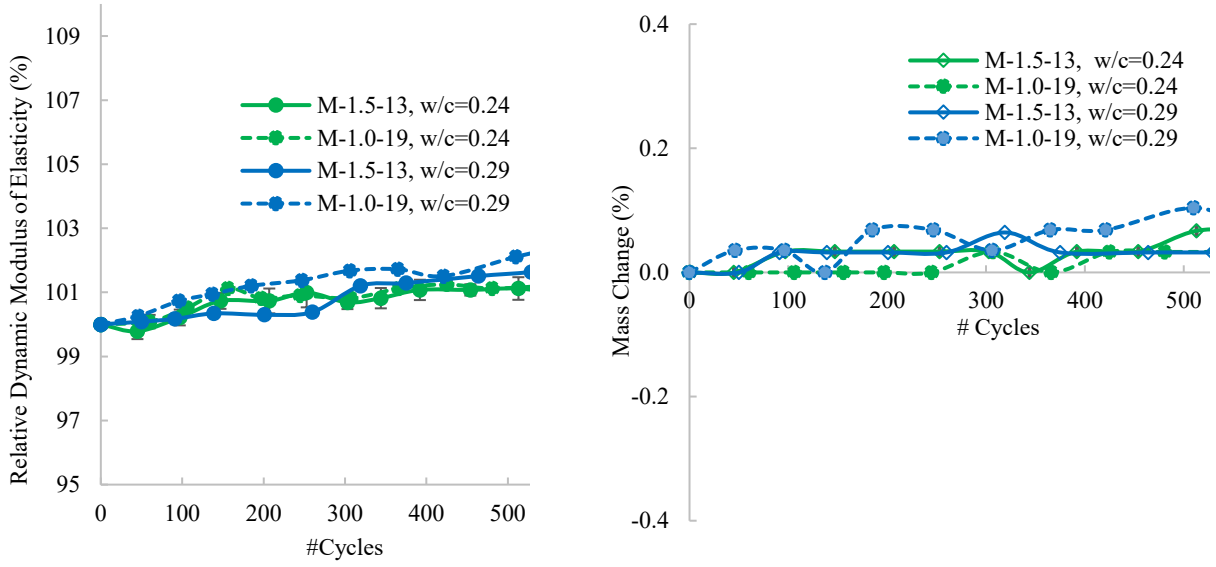

(a) Relative dynamic modulus of elasticity (b) Mass change (%)

Figure 20: Freeze-thaw resistance of fiber reinforced UHPCs

3.6.3. Comparison of freeze-thaw results with other researchers

The comparative summary of freeze-thaw resistance results from previous studies [33–36,41,42,45,49–53]are presented in **Figure 21**. The green dots represent non-proprietary UHPCs, while yellow dots represent proprietary UHPCs. RDME is plotted against different F-T cycles. The

current study measured RDME after 600 F-T cycles, which is observed to be comparatively higher than those from most previous studies, except one dataset. There is no significant difference between RDMEs from proprietary and non-proprietary UHPCs. The absence of deterioration signs in UHPC specimens, even after 600 freeze–thaw cycles, indicates low water absorption into the sample due to the presence of smaller gel pores, signifying a dense matrix [50].

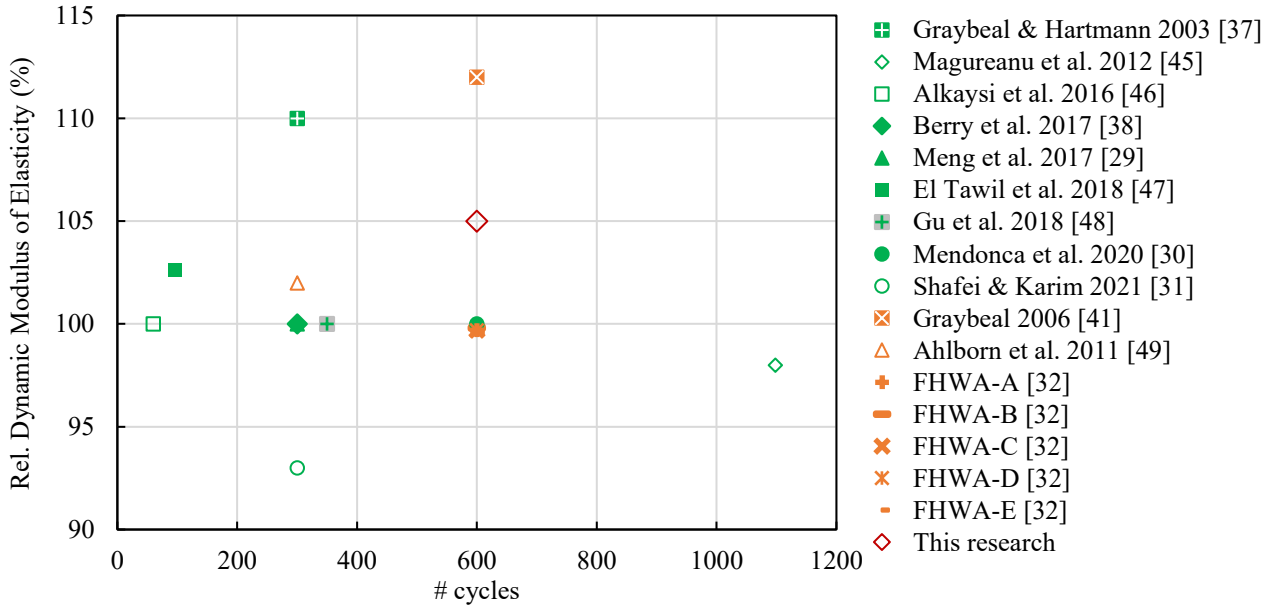

Figure 21: Summary of freeze-thaw resistance of UHPCs

3.7. Service life modeling from electrical surface resistivity

Several software programs can model the service life of concrete structures, including Life 365, ConcreteWorks, and STADIUM. Among these, Life 365 is quite popular. It considers factors such as the percentage of SF and GGBS, as well as the W/C ratio. Other exposure conditions are based on the geographical location of the structures. Life 365 promotes the use of SF and GGBS, as increasing their percentage in the mixture design is said to lengthen the service life of concrete structures. However, this may lead to an overestimation of the service life for concrete mixtures containing SF and GGBS. Additionally, Life 365 was designed to model the service life of structures built with normal concrete and does not account for the specific characteristics of UHPC, such as low W/C ratios (less than 0.25), particle packing principle, fine aggregates, or the use of glass powder or quartz powder. Furthermore, it only considers class FA F. Therefore, this software is insufficient for accurately modeling the service life of a UHPC structure.

Another promising way to determine the service life of concrete is using the error function solution to Fick's second law. According to this law of diffusion, the rate at which ions move through a material is proportional to the concentration gradient between its two ends [54].

Change in concentration (C) per unit time = change in flux per unit distance

$$\frac{\partial C}{\partial t} = -\frac{\partial J}{\partial x} \tag{7}$$

$$\text{By replacing flux } J = -D\frac{\partial C}{\partial x}, \frac{\partial C}{\partial t} = -\frac{\partial}{\partial x}(-D\frac{\partial C}{\partial x})$$

$$\frac{\partial C}{\partial t} = D\frac{\partial^2 C}{\partial x^2}$$

Using the Gaussian error function in the above equation, the solution becomes

$$C(x,t) = A + B \times \text{erf}\,(\frac{x}{2\sqrt{Dt}}) \tag{8}$$

where A and B are constant based on the boundary conditions. The formation factor and self-diffusion coefficient can replace the original diffusion coefficient in the error function solution using the Nernst–Einstein relationship, formulated as follows [55]:

$$\frac{C_{x,t} - C_o}{C_s - C_o} = 1 - \text{erf}\left(\frac{x}{2\sqrt{\frac{t \times D_o}{F}}}\right) \tag{9}$$

, where

$C_{x,t}$ = Chloride concentration at depth x (%) = 0.05%

C_o = Initial chloride concentration (%) = 0.02%

C_s = Surface chloride concentration (%) = 0.68%

x = Depth to reinforcement (in) = 2 in cover

D_o = Chloride ion self-diffusion coefficient (in/s2) = 19×10^{-10} m^2/s

F = Formation factor

t = Time for exposure limit to be reached (s).

All constants are based on the exposure region. For example, for an urban highway bridge in Bridgeport, Connecticut that carries interstate highways and is exposed to marine conditions, specific values are available.

The formation factor can be determined as per AASHTO PP84 [56]:

$$\text{Formation factor } F = \frac{BR}{PSR} \tag{10}$$

, where bulk resistivity (BR) can be calculated from surface resistivity (SR) using an equation provided by Spragg et al. 2013 [57], and pore solution resistivity (PSR) can be obtained from software developed by NIST based on Snyder et al. 2003 [58] with 40% hydration after 28 days or considered as 0.05 Ω·m for UHPC [55].

$$\frac{SR}{BR} = 1.10 - \frac{0.730}{\frac{d}{a}} + \frac{7.34}{(\frac{d}{a})^2} \tag{11}$$

, where d and a refer to diameter and probe spacing, respectively. In this study, d = 76 mm and a = 38 mm. Thus, this equation becomes

$$BR = \frac{SR}{2.57} \tag{12}$$

Additionally, corrosion rate ($V_{corr.}$) can be predicted from an empirical formula [59]:

$$V_{corr.} = \frac{301.6}{BR} \text{ mm/year} \tag{13}$$

, where BR is in Ω·m.

After substituting all values into **Equation (9)**, time is calculated in seconds and then converted to years.

Table 5 shows the calculated service life based on **Equations (9)** to **(12)** and the assumptions described above. The results show that M can last for 376 years, M-0.2SF for 345 years, and M-RGP for 383 years, while M-0.3GGBS only lasts for 147 years. Since GGBS delays the hydration reaction, it takes longer to develop a denser microstructure, resulting in lower electrical surface resistivity at 28 days, which ultimately impacts the service life prediction. This service life can be expected to be even higher, around 550–600 years, if the depth of cover is increased from 2 inches to 2.5 inches. Two inches of cover was considered to calculate service life to remain conservative. This indicates that service life predictions can vary based on the assumptions made for calculations or real-world circumstances.

Table 5: Service life prediction based on Fick's second law

Mix	Diffusion Coefficient	Formation Factor	Predicted Service Life	Corrosion Rate (m/year)
M	2.90×10^{-14} m²/s	65,510	376	0.92×10^{-6} m/year
M-0.2SF	3.16×10^{-14} m²/s	60,048	345	1.0×10^{-6} m/year
M-RGP	2.85×10^{-14} m²/s	66,693	383	0.90×10^{-6} m/year
M-0.3GGBS	7.43×10^{-14} m²/s	25,577	147*	2.35×10^{-6} m/year

* Since SR is less than other UHPCs after 28 days, which eventually becomes 1000 kΩ·cm.

The results presented here are similar to those in previous research [60], with the primary difference being the aggregate-to-cement ratios. This study has shown slightly higher electrical surface resistivity over the same period.

Further detailed implications and techno-economic analysis were performed and presented their results in authors' new publication [61].

Chapter 4: Conclusions and Recommendations

In this research durability properties of newly developed, resource-efficient non-proprietary UHPCs were investigated and characterized. The service life was determined. The following conclusions have been drawn from this research.

1. **Freeze-thaw resistance**: All the newly developed non-proprietary UHPCs (with and without fibers) exceeded an RDME of 100% even after 600 F-T cycles. The increase in dynamic modulus is attributed to the hydration reaction during thawing cycles when the temperature becomes positive. Additionally, F-T test following ASTM C666 provides a reliable indication of the durability of concrete mixtures.
2. **Permeability:** All newly developed non-proprietary UHPCs (with and without fibers) exceeded the low permeability threshold limit (electrical surface resistivity over 21 kΩ·cm) in less than a month. However, the inclusion of steel fibers affected electrical surface resistivity. Fiber-reinforced UHPCs showed lower electrical surface resistivity values than those without fibers. This suggests that electrical resistivity is a suitable tool for characterizing the durability performance of UHPC matrices without fiber reinforcement. For fiber-reinforced UHPCs, further investigation is recommended to develop empirical formulas and relationships that facilitate durability assessment through electrical resistivity measurements.
3. **Drying shrinkage:** UHPCs without fibers and a W/C ratio of 0.24 showed an average drying shrinkage of 1000 με in about two months. The same UHPC mixture with fibers of two different fiber lengths (13 mm and 19 mm, both with a diameter of 0.2 mm) showed less than 600 με of drying shrinkage in the same period. UHPCs with fibers and a W/C ratio of 0.29 exhibited less than 1000 με within two months.
4. **Absorption:** The absorption of UHPCs was found to be less than 1.4% after 28 days of curing, attributed to the dense microstructure.

5. **Large scale mix with casting delay:** Casting delays had a significant impact on the workability of the UHPC mix. One hour and two hours of delay caused the static flow to drop by 37% to 175 mm from 276 mm and by 47% to 148 mm, respectively. The compressive strength of the mixes was not significantly affected by the casting delay. The samples without delay had an average 28-day compressive strength of 155 MPa while the samples with 1 and 2 hours of delay had an average 28-day compressive strength of 166 and 156 MPa, respectively. All samples showed strain hardening behavior with an average ultimate tensile strength ranging from 11 to 14 MPa and hardening strain from 0.21-0.28%.
6. **Service life:** The estimated service life of these non-proprietary UHPCs is approximately 350 years, based on chloride diffusion theory. This assumes bridge infrastructure in an urban, marine environment in Bridgeport, Connecticut, though factors like climate change may alter projections.

References

[1] O.F.A. INFRASTRUCTURE, A comprehensive assessment of America's infrastructure, in: ASCE Reston, VA, 2021.

[2] A.S. of C. Engineers, Failure to Act: Closing the Infrastructure Investment Gap for America's Economic Future, in: American Society of Civil Engineers, 2016.

[3] J. Li, Z. Wu, C. Shi, Q. Yuan, Z. Zhang, Durability of ultra-high performance concrete – A review, Constr Build Mater 255 (2020) 119296. https://doi.org/https://doi.org/10.1016/j.conbuildmat.2020.119296.

[4] B. 'Rai, K. 'Wille, R. 'Malla, Development and Testing of High / Ultra-High Early Strength Concrete for durable Bridge Components and Connections, 2022.

[5] E. Sakai, N. Akinori, M. Daimon, K. Aizawa, H. Kato, Influence of Superplasticizer on the Fluidity of Cements with Different Amount of Aluminate Phase, in: Second International Symposium on Ultra High Performance Concrete, Kassel, 2008: pp. 85–92.

[6] ASTM C150, Standard Specification for Portland Cement, Annual Book of ASTM Standards (2007). www.astm.org.

[7] ASTM C618, Standard Specification for Coal Fly Ash and Raw or Calcined Natural Pozzolan for Use in Concrete, Annual Book of ASTM Standards (2022). https://doi.org/10.1520/C0618-22.

[8] K. Wille, A.E. Naaman, G.J. Parra-Montesinos, Ultra-High Performance Concrete with Compressive Strength Exceed 150 MPa (22 ksi): A Simpler Way, 2009.

[9] B. Rai, C. Boisvert-Cotulio, K. Wille, Resource-efficient design of ultra-high performance concretes, Journal of Building Engineering (2024) 109630. https://doi.org/10.1016/j.jobe.2024.109630.

[10] ASTM C230, Standard Specification for Flow Table for Use in Tests of Hydraulic Cement, (2008). www.astm.org,.

[11] K. Wille, A.E. Naaman, G.J. Parra-Montesinos, Ultra-High Performance Concrete with Compressive Strength Exceeding 150 MPa (22 ksi): A Simpler Way, ACI Mater J 108 (2011) 34–46.
[12] Standard Specification for Flow Table for Use in Tests of Hydraulic Cement https://doi.org/10.1520/C0230_C0230M-21.
[13] Standard Test Method for Flow of Hydraulic Cement Mortar 1, n.d. www.astm.org.
[14] Standard Test Method for Compressive Strength of Hydraulic Cement Mortars (Using 2-in. or [50-mm] Cube Specimens) 1, n.d.
[15] K. Wille, S. El-Tawil, A.E. Naaman, Properties of strain hardening ultra high performance fiber reinforced concrete (UHP-FRC) under direct tensile loading, Cem Concr Compos 48 (2014) 53–66. https://doi.org/https://doi.org/10.1016/j.cemconcomp.2013.12.015.
[16] ASTM C642-21: Standard Test Method for Density, Absorption, and Voids in Hardened Concrete, (2022). https://doi.org/10.1520/C0642-21.
[17] AASHTO-T95 Standard Test Method for Surface Resistivity of Concrete's Ability to Resist Chloride Ion Penetration, American Association of State Highway and Transportation Officials (2014) 10.
[18] M. Kamali, A. Ghahremaninezhad, An investigation into the hydration and microstructure of cement pastes modified with glass powders, Constr Build Mater 112 (2016) 915–924.
[19] Surface Electrical Resistivity of Concrete, n.d. www.giatec.ca.
[20] ASTM C157/C157M-17, Standard Test Method for Length Change of Hardened Cement Mortar And Concrete, Annual Book of ASTM Standards (2017). https://doi.org/10.1520/C0157_C0157M-17.
[21] ASTM C666/C666M-03: Standard Test Method for Resistance of Concrete to Rapid Freezing and Thawing, ASTM International, 2003.
[22] ASTM C215-19, Standard Test Method for Fundamental Transverse, Longitudinal, and Torsional Resonant Frequencies of Concrete Specimens, Annual Book of ASTM Standards (2019). https://doi.org/10.1520/C0215-19.
[23] N. Roux, C. Andrade, M.A. Sanjuan, EXPERIMENTAL STUDY OF DURABILITY OF REACTIVE POWDER CONCRETES, Journal of Materials in Civil Engineering 8 (1996) 1–6.
[24] M.G. Sohail, R. Kahraman, N. Al Nuaimi, B. Gencturk, W. Alnahhal, Durability characteristics of high and ultra-high performance concretes, Journal of Building Engineering 33 (2021). https://doi.org/10.1016/j.jobe.2020.101669.
[25] C.M. Tam, V.W.Y. Tam, K.M. Ng, Assessing drying shrinkage and water permeability of reactive powder concrete produced in Hong Kong, Constr Build Mater 26 (2012) 79–89. https://doi.org/10.1016/j.conbuildmat.2011.05.006.
[26] Z. Liu, S. El-Tawil, W. Hansen, F. Wang, Effect of slag cement on the properties of ultra-high performance concrete, Constr Build Mater 190 (2018) 830–837. https://doi.org/10.1016/j.conbuildmat.2018.09.173.
[27] R.S. Edwin, M. de Schepper, E. Gruyaert, N. de Belie, Effect of secondary copper slag as cementitious material in ultra-high performance mortar, Constr Build Mater 119 (2016) 31–44. https://doi.org/10.1016/j.conbuildmat.2016.05.007.
[28] B. Rai, K. Wille, Time-dependent properties of steam cured non-proprietary ultra high-performance concretes, Case Studies in Construction Materials 20 (2024). https://doi.org/10.1016/j.cscm.2023.e02760.

[29] S. Cleven, M. Raupach, T. Matschei, Electrical resistivity of steel fibre-reinforced concrete—influencing parameters, Materials 14 (2021). https://doi.org/10.3390/ma14123408.
[30] A. Miri, R. Ehsani, F.M. Tehrani, A Numerical Simulation of Electrical Resistivity of Fiber-Reinforced Composites, Part 1: Brittle Cementitious Concrete, Modelling 3 (2022) 164–176. https://doi.org/10.3390/modelling3010011.
[31] A. Malakooti, R.J. Thomas, M. Maguire, INVESTIGATION OF CONCRETE ELECTRICAL RESISTIVITY AS A PERFORMANCE-BASED TEST, Salt Lake City, 2019. www.udot.utah.gov/go/research.
[32] B. Dong, J. Zhang, Y. Wang, G. Fang, Y. Liu, F. Xing, Evolutionary trace for early hydration of cement paste using electrical resistivity method, Constr Build Mater 119 (2016) 16–20. https://doi.org/10.1016/j.conbuildmat.2016.03.127.
[33] W. Meng, M. Valipour, K.H. Khayat, Optimization and performance of cost-effective ultra-high performance concrete, Materials and Structures/Materiaux et Constructions 50 (2017). https://doi.org/10.1617/s11527-016-0896-3.
[34] F.E.-K.M. Mendonca, G. Morcous, J. Hu, Feasibility Study of Development of Ultra-High Performance Concrete (UHPC) for Highway Bridge Applications in Nebraska. SPR-P1(18) M072., 2020. https://digitalcommons.unl.edu/ndor/242.
[35] B. Shafei, R. Karim, Development of Non-Proprietary Ultra-High Performance Concrete (UHPC) for Iowa Bridges final report. IHRB Project TR-773., 2021. https://bec.iastate.edu.
[36] FHWA-HRT-18-036, FHWA Report: Properties and Behavior of UHPC-Class Materials. FHWA Publication No: FHWA-HRT-18-036., 2018. https://www.fhwa.dot.gov/publications/research/infrastructure/structures/bridge/18036/18036.pdf.
[37] A. Itim, K. Ezziane, E.H. Kadri, Compressive strength and shrinkage of mortar containing various amounts of mineral additions, Constr Build Mater 25 (2011) 3603–3609. https://doi.org/10.1016/j.conbuildmat.2011.03.055.
[38] K.M. Lee, H.K. Lee, S.H. Lee, G.Y. Kim, Autogenous shrinkage of concrete containing granulated blast-furnace slag, Cem Concr Res 36 (2006) 1279–1285. https://doi.org/10.1016/j.cemconres.2006.01.005.
[39] Tazawa E., S. Miyazawa, Influence of constituents and composition on autogenous shrinkage of cementitious materials, Magazine of Concrete Research 49 (1997) 15–22.
[40] J. Yuan, W. Lindquist, D. Darwin, J.A. Browning, Effect of slag cement on drying shrinkage of concrete, ACI Mater J 112 (2015) 267–276. https://doi.org/10.14359/51687129.
[41] B.A. Graybeal, J.L. Hartmann, STRENGTH AND DURABILITY OF ULTRA-HIGH PERFORMANCE CONCRETE, in: Concrete Bridge Conference, 2003. https://www.researchgate.net/publication/265243898.
[42] M. Berry, R. Snidarich, C. Wood, Development of Non-Proprietary Ultra-High Performance Concrete, 2017. https://rosap.ntl.bts.gov/view/dot/35953.
[43] L. Teng, M. Valipour, K.H. Khayat, Design and performance of low shrinkage UHPC for thin bonded bridge deck overlay, Cem Concr Compos 118 (2021). https://doi.org/10.1016/j.cemconcomp.2021.103953.
[44] Y. Aljawad, R.D. Lequesne, M. O'reilly, SL Report 22-3: LOW-SHRINKAGE ULTRA-HIGH-PERFORMANCE CONCRETE, Lawrence, Kansas, 2022. http://hdl.handle.net/1808/33326.
[45] B.A. Graybeal, FHWA Report: Material Property Characterization of Ultra-High Performance Concrete. FHWA Publication No: FHWA-HRT-06-103, 2006. https://www.fhwa.dot.gov/publications/research/infrastructure/structures.

[46] F. Roberti, V.F. Cesari, P.R. de Matos, F. Pelisser, R. Pilar, High- and ultra-high-performance concrete produced with sulfate-resisting cement and steel microfiber: Autogenous shrinkage, fresh-state, mechanical properties and microstructure characterization, Constr Build Mater 268 (2021). https://doi.org/10.1016/j.conbuildmat.2020.121092.
[47] S. Jacobsen, E.J. Sellevold, SELF HEALING OF HIGH STRENGTH CONCRETE AFTER DETERIORATION BY FREEZE/THAW, Cem Concr Res 26 (1996) 55–62.
[48] B. Graybeal, J. Tanesi, Durability of an Ultra high-Performance Concrete Durability of an Ultrahigh-Performance Concrete, Journal of Materials in Civil Engineering 19 (2007) 848–854. https://doi.org/10.1061/ASCE0899-1561200719:10848.
[49] C. Magureanu, I. Sosa, C. Negrutiu, B. Heghes, Mechanical Properties and Durability of Ultra-High-Performance Concrete, ACI Mater J 109 (2012) 177–183. https://doi.org/10.14359/51683704.
[50] M. Alkaysi, S. El-Tawil, Z. Liu, W. Hansen, Effects of silica powder and cement type on durability of ultra high performance concrete (UHPC), Cem Concr Compos 66 (2016) 47–56. https://doi.org/10.1016/j.cemconcomp.2015.11.005.
[51] S. El-Tawil, M. Alkaysi, A.E. Naaman, W. Hansen, Z. Liu, Development, Characterization and Applications of a Non Proprietary Ultra High Performance Concrete for Highway Bridges, 2016.
[52] C. Gu, W. Sun, L. Guo, Q. Wang, J. Liu, Y. Yang, T. Shi, Investigation of Microstructural Damage in Ultrahigh-Performance Concrete under Freezing-Thawing Action, Advances in Materials Science and Engineering 2018 (2018). https://doi.org/10.1155/2018/3701682.
[53] T.M. Ahlborn, D.K. Harris, D.L. Misson, E.J. Peuse, Characterization of strength and durability of ultra-high-performance concrete under variable curing conditions, Transp Res Rec (2011) 68–75. https://doi.org/10.3141/2251-07.
[54] A. Fick, On liquid diffusion, J Memb Sci 100 (1995) 33–38. https://doi.org/https://doi.org/10.1016/0376-7388(94)00230-V.
[55] K.A. Snyder, The relationship between the formation factor and the diffusion coefficient of porous materials saturated with concentrated electrolytes: theoretical and experimental considerations, Concrete Science and Engineering 3 (2001) 216–224. https://tsapps.nist.gov/publication.
[56] AASHTO PP 84-18, Standard Practice for Developing Performance Engineered Concrete Pavement Mixtures, (2018). https://www.techstreet.com/standards/aashto-pp-84-18.
[57] R. Spragg, Y. Bu, K. Snyder, D. Bentz, J. Weiss, Electrical Testing of Cement-Based Materials: Role of Testing Techniques, Sample Conditioning, and Accelerated Curing, 2013. https://doi.org/10.5703/1288284315230.
[58] K.A. Snyder, X. Feng, B.D. Keen, T.O. Mason, Estimating the electrical conductivity of cement paste pore solutions from OH-, K+ and Na+ concentrations, Cem Concr Res 33 (2003) 793–798. https://doi.org/10.1016/S0008-8846(02)01068-2.
[59] C. Andrade, Design and evaluation of service life through concrete electrical resistivity, Revista ALCONPAT 8 (2018) 264–279. https://doi.org/10.21041/ra.v8i3.349.
[60] B. Rai, K. Wille, Recycled glass powder as an alternative to fly ash in non-proprietary UHPC: A comparative study of resource-efficient design, mechanical and durability properties, J Clean Prod (2023). https://doi.org/10.1016/j.jclepro.2024.141907.
[61] B. Rai, K. Wille, Durability, Service Life, and Techno-Economic Analysis of Non-Proprietary UHPC, Fibers 13 (2025) 22. https://doi.org/10.3390/fib13020022.

Transportation Infrastructure Durability Center
AT THE UNIVERSITY OF MAINE

35 Flagstaff Road
Orono, Maine 04469
tidc@maine.edu
207.581.4376

www.tidc-utc.org